# Pattern Formation in Mesophase Carbon Fibers

Lei Wang

Department of Mathematics and Statistics

McGill University, Montreal

July 1996

A Thesis submitted to the Faculty of Graduate Studies and Research in partial fulfiment of the requirements for the degree of Master of Science

© Lei Wang 1996. All rights reserved.

National Library of Canada
Acquisitions and Bibliographic Services Branch
395 Wellington Street
Ottawa, Ontario
K1A 0N4

Bibliothèque nationale du Canada
Direction des acquisitions et des services bibliographiques
395, rue Wellington
Ottawa (Ontario)
K1A 0N4

*Your file* *Votre référence*

*Our file* *Notre référence*

**The author has granted an irrevocable non-exclusive licence allowing the National Library of Canada to reproduce, loan, distribute or sell copies of his/her thesis by any means and in any form or format, making this thesis available to interested persons.**

**L'auteur a accordé une licence irrévocable et non exclusive permettant à la Bibliothèque nationale du Canada de reproduire, prêter, distribuer ou vendre des copies de sa thèse de quelque manière et sous quelque forme que ce soit pour mettre des exemplaires de cette thèse à la disposition des personnes intéressées.**

**The author retains ownership of the copyright in his/her thesis. Neither the thesis nor substantial extracts from it may be printed or otherwise reproduced without his/her permission.**

**L'auteur conserve la propriété du droit d'auteur qui protège sa thèse. Ni la thèse ni des extraits substantiels de celle-ci ne doivent être imprimés ou autrement reproduits sans son autorisation.**

ISBN 0-612-19855-3

Canada

*To my parents*

# Foreword

The present author chooses the manuscript-based thesis option according to the following thesis preparation guideline given by the Faculty of Graduate Studies and Research:

*Candidates have the option of including, as part of the thesis, the text of a paper(s) submitted or to be submitted for publication, or the clearly-duplicated text of a published paper(s). These texts must be bound as an integral part of the thesis.*

*If this option is chosen, connecting texts that provide logical bridges between the different papers are mandatory. The thesis must be written in such a way that it is more than a mere collection of manuscripts; in other words, results of a series of papers must be integrated.*

*The thesis must still conform to all other requirements of the "Guidelines for Thesis Preparation". The thesis must include: A Table of Contents, an abstract in English and French, an introduction which clearly states the rationale and objectives of the study, a comprehensive review of the literature, a final conclusion and summary, and a thorough bibliography or reference list.*

*Additional material must be provided where appropriate (e.g. in appendices) and in sufficient detail to allow a clear and precise judgement to be made of the importance and originality of the research reported in the thesis.*

*In the case of manuscripts co-authored by the candidate and others, the candidate is required to make an explicit statement in the thesis as to who contributed to such work and to what extent. Supervisors must attest to the accuracy of such statements at the doctoral oral defense. Since the task of the examiner is made more difficult in these cases, it is in the candidate's interests to make perfectly clear the responsibilities of all the authors of co-authored papers. Under no circumstances can a co-author of any component of such a thesis serve as an examiner for that thesis.*

Contents of Chapters 2 and 3 of the present thesis are adopted from the papers that have been submitted, or will be submitted shortly for publication in scientific journals under normal supervisor of my research supervisor, Professor A.D.Rey, who is also the co-author.

I, Alejandro D. Rey, hereby give copyright clearance of the following papers, of which I am the co-author, in the thesis of Lei Wang.

1. Chapter 2: L. Wang and A.D. Rey, "Pattern formation and non-linear phenomena in stretched discotic liquid crystal fibers", submitted to Physical Review E (1996).

2. Chapter 3: L. Wang and A.D. Rey, "Pattern selection mechanisms in mesophase carbon fibers", submitted to Modelling and Simulation in Material Science and Engineering (1996).

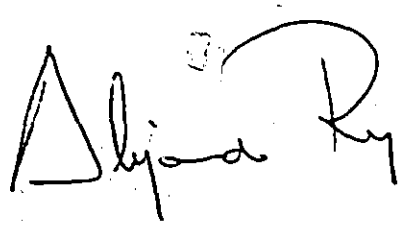

Professor Alejandro D. Rey
Department of Chemical Engineering
McGill University
Montreal, PQ

# Pattern Formation in Mesophase Carbon Fibers


## Abstract

The principles governing pattern formation in discotic nematic liquid crystalline fibers subjected to uniaxial extensional flows are established. Computational and analytical methods are used in conjunction with bifurcational techniques to simulate the structural characteristics of the orientational patterns that arise by stretching discotic nematic liquid crystalline materials. The analytical and numerical results are in excellent agreement with actual cross-sectional fiber textures obtained by melt spinning carbonaceous mesophases. This work reproduces the main structural features of the oscillatory zig-zag pattern commonly observed in mesophase carbon fibers, and identifies the process conditions that lead to this peculiar fiber texture. In addition, the temperature driven texture transitions and the emergence of a random pattern also observed during the industrial manufacturing of mesophase carbon fibers are captured by the simulations and thoroughly explained using classical viscoelastic theories of liquid crystalline materials.

# Arrangement moléculaire dans les Fibres Mesophases de Carbone


## Résumé

Les principes qouvernant l'arrangement des molécules dans les fibres discotiques nématiques cristallins liquids soumisent à des écoulements uniaxials extensionnels ont été étudiés. Des méthodes numériques et analytiques ont été utilisées avec l'aide de techniques de bifurcation pour simuler les caractéristiques structurelles des arrangement molécularies qui surviennent lors de l'étirement des matériaux nématiques discotiques cristallins liquides. Les résultats obtenus par les techniques ci-haut mentionnées sont en excellent accord avec ceux des textures de véritables fibres formées par le procédé de tournage de fibres mésophases liquides de carbone. Cette étude reproduit les principales caractéristiques structurelles de l'arrangement zigzag oscillatoire qui cont souvent observées dans les fibres mésophases de carbone et identifie les conditions de procédé qui mènent à cette texture particulière des fibres. En plus, l'effet de la température sur les changements de textures et l'apparition d'arrangements aléatoires ont aussi été expliqués en utilisant les théories classiques des matériaux viscoélastiques liquides cristallins.

# Acknowledgments

It is a great pleasure to express my deepest gratitude to my thesis supervisor, Professor Alejandro D. Rey, for his inspiring guidance, support and constant encouragement all through the course of my work. I learned from him not only knowledge but more importantly his dedication.

I would also like to thank the members of Dr. Rey's research group, Tao Huang, Philip Chan, Arvinder Singh for all the help they gave me. Special thanks to François Godin for translating the abstract into french.

Finally, I wish to thank my family for their love and support.

# Contents

# List of Figures

# Chapter 1

# Introduction

## 1.1 Carbon Fibers

The three different types of commercial carbon fibers, manufactured from three different precursor materials, are: rayon carbon fibers, acrylic carbon fibers, and mesophase pitch-based carbon fibers [1][2]. The rayon carbon fibers have relatively low tensile strength and low Young's modulus, and have been used mainly as composites designed for use in rocket and space shuttle applications. The acrylic carbon fibers commonly known as PAN-based (poly-acrylonitrile) carbon fibers are copolymers containing acrylonitrile in excess of 85% along with other co-monomers which are used to improve processability. The PAN-based carbon fibers have high strength, high modulus and semi-conducting properties and are used in a wide variety of applications [2-5]. Pitch-based carbon fibers can be manufactured from two different states of the same precursor material (coal or petroleum pitches): the liquid crystalline (discotic) state or mesophase, and the isotropic state. The isotropic pitch-based carbon fibers have low modulus and strength. The mesophase pitch-based carbon fibers have ultrahigh strength and modulus, and can be used in the same applications as PAN-based carbon fibers. In addition, mesophase pitch-based carbon fibers have high thermal and electrical conductivities and are often used in high thermal transport applications. This thesis is restricted to the study of mesophase pitch-based carbon fibers.

The industrial production of mesophase carbon fibers uses the so called melt-spinning

process. Fig. 1-1 shows an schematic of actual spinning process of mesophase carbon fibers [6]. Typically, the precursor carbonaceous mesophase pitch is melted in an extruder which then pumps the melt into the spin pack. The molten pitch is filtered to remove solid impurities before being extruded through a spinnerette. The pitch is subjected to high extensional and shear stresses as it approaches and flows through the spinnerette capillaries. The associated flow-induced torques tend to orient the molecules in a regular transverse pattern. Upon emerging from the spinnerette capillaries, the as-spun fibers are drawn to improve axial orientation and are collected on a wind-up device. The basic microstructure of fibers is formed during the spinning and drawing processes.

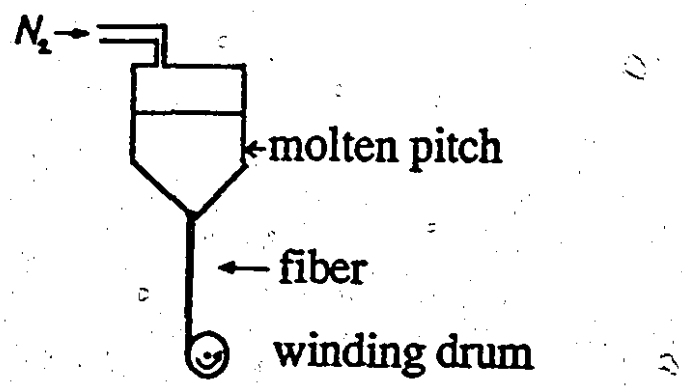


Figure 1-1: Schematic diagram of melt-spinning process of mesophase carbon fibers

The carbon fibers melt-spun from mesophase pitch through such process exhibit a variety of transverse textures. The microstructure of the fibers is defined by the spatial arrangement of the flat disc-like molecules in the fibers. Figure 1-2 shows a scanning electron micrograph of the cross-section of a mesophase carbon fiber [7]. The characteristic feature of Fig. 1-2 is the radial oscillatory orientation. Other patterns, known as radial pattern, onion pattern and random pattern are also observed in the cross-section of fibers, as shown in Fig. 1-3 [8]. These three patterns are observed on the cross-section of carbon fibers spun at different temperatures. Figure 1-4 [9] shows the correlation between temperature and the radial, onion and random transverse textures. All these patterns correspond to different states of molecular order prevailing in that mesophase

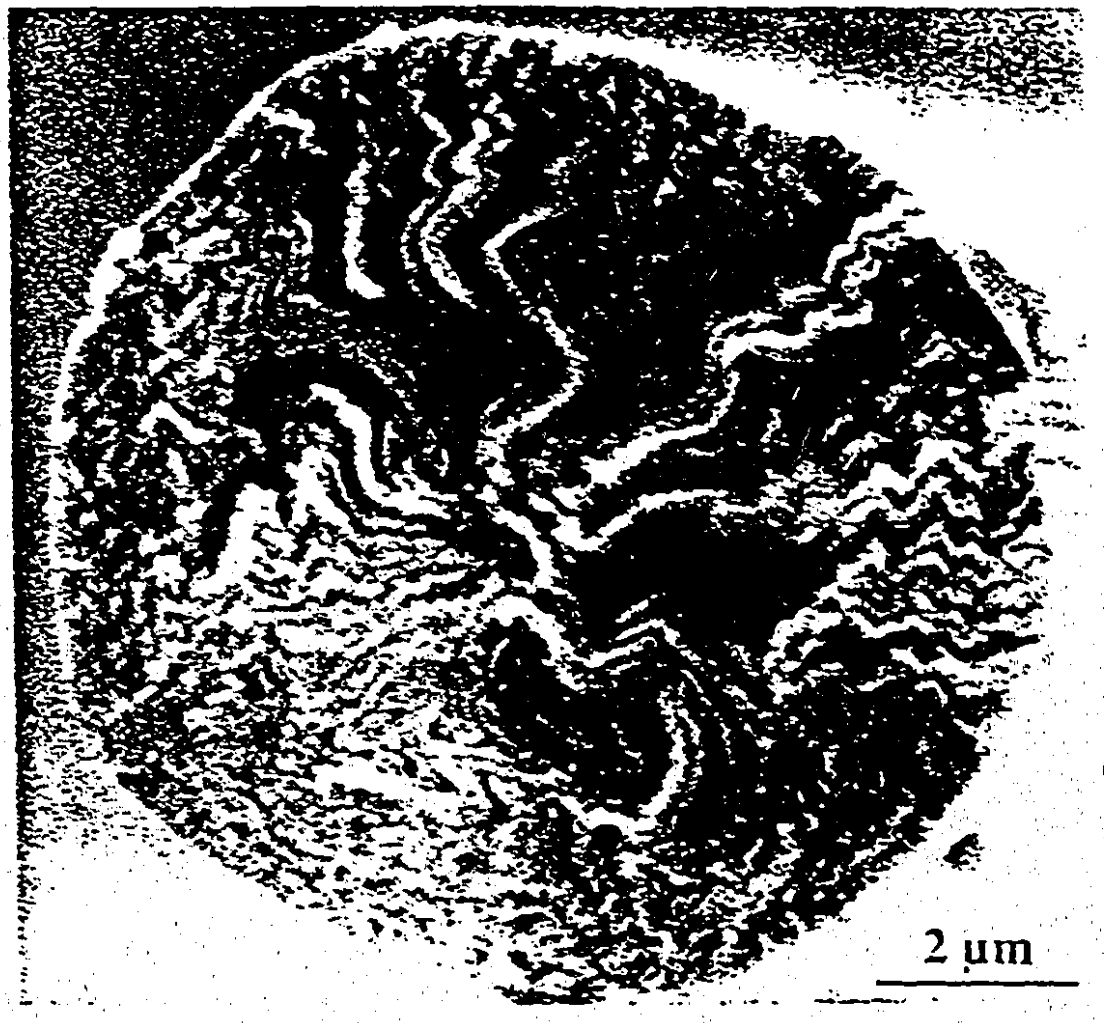


Figure 1-2: Scanning electron micrograph of the fracture surface of a mesophase carbon fiber displaying a radial oscillatory transverse texture, adopted from [7].

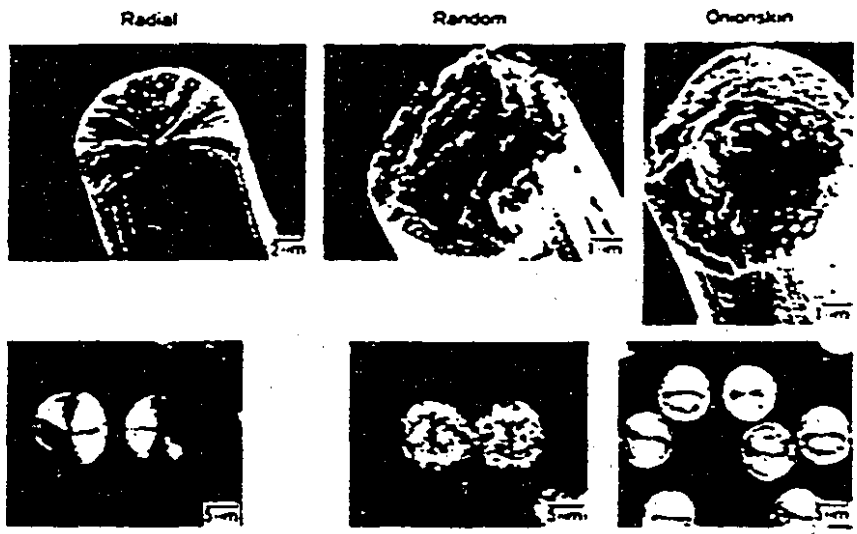


Figure 1-3: (Top row) Micrographs of fracture surfaces of as-spun mesophase pitch fibers and (bottom row) polarized light photomicrographs of polished transverse sections of radial, onion, and random structures, adopted from [8].

and thus represent different microstructures of the fibers, but the origin of such patterns and the selection mechanism that promotes the formation of particular patterns in the fiber spinning of carbonaceous mesophases are currently not well understood. Since the cross-sectional patterns of carbon fibers are closely related to their physical properties. the control of the pattern formation in these fibers is essential to optimize the product property profile. This thesis uses theory and simulation to reproduce and explain the basic microstructural features shown in the radial texture (Figure 1-2), and the radial, random and onion patterns shown in Fig. 1-3. The remainder of this introductory chapter presents the basic concepts and theories used to simulate and explain the pattern formation in the melt-spinning of carbonaceous mesophases, as described above.

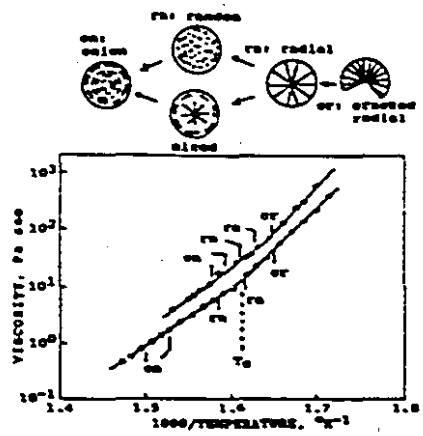

Figure 1-4: Variation of mesophase fiber texture with melt spinning temperature, adopted from [9].

## 1.2 Discotic Nematic Liquid Crystals

For many organic compounds the phase transition between the solid state and liquid state is not a single phase transition, an intermediate state called mesophase (i.e. intermediate phase) is developed in between solid and liquid [11]. The mesomorphic materials possess both liquid-like fluidity and solid-like molecular order. In solid crystals the center of mass of the molecules are located on a three dimensional periodic lattice, hence they have both orientational as well as positional order. In the case of isotropic liquids only short range order among the molecular centers of mass is present. The ordering in mesophases (mesomorphic or anisotropic liquids) lies between that of a solid and that of an isotropic liquid. Based on the partial ordering two basically different types of mesophases have been observed. First type shows a transition from a strongly ordered state to a phase where each molecule commutes between several equivalent orientations. The positional order is still present but the orientational order has disappeared or is strongly reduced. and this phase is called disordered crystal mesophases or plastic crystal. The second type shows a low temperature phase where the positional order is reduced or has even completely disappeared but exhibit long range orientational order, and this phase is called ordered fluid mesophase or liquid crystal. At higher temperatures, liquid crystals undergo a transition to a conventional (isotropic) liquid. The shape of the molecule is an important factor for mesomorphism to occur. Two types of liquid crystals compounds

characerized by the shapes of their molecules are most widely studied, the rod-like liquid crystals and disk-like liquid crystals, also known as discotic liquid crystals.

Based on the classification by Friedel in 1922, liquid crystals are categorized according to their molecular order into three major classes: nematic, cholesteric , and smectic. In nematic liquid crystals, considered in this thesis, the molecules tend to align parallel to each other and along some common axis called director. The director is a unit vector **n**, and it gives the average preferred orientation. Long range orientational order and cylindrical (uniaxial) symmetry are often exhibited by this type of liquid crystal phase. The center of gravity of the molecules are distributed at random. Therefore such liquid crystals possess orientaional order like crystals and positional disorder like viscous phase. When the constituent molecules are of disk-like shape, the resulting phase is called discotic nematic liquid crystal. Figure 1-5 shows a schematic of orientational ordering of discotic nematic liquid crystals. The short arrows are the molecular unit normals to the disc-like molecules, and they orient more or less parallel to the average orientation **n**.

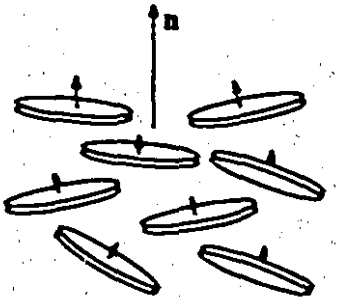


Figure 1-5: Orientational ordering in the uniaxial discotic nematic phase. The molecular normals of the randomly positioned disk-like molecules partially orient along the director **n**.

The carbonaceous mesophase studied in this thesis is a uniaxial discotic nematic liquid crystalline thermodynamic phase, which forms during the liquid phase pyrolysis of coal or petroleum pitches. When heating a non-volatile organic compound, such as coal or petroleum pitch, in the absence of air, the thermodynamic and structural change are as follows. First the organic substance melts on heating and becomes isotropic pitch or

liquid. As the temperature rises over about 350°C, optically anisotropic spheres, known as spherules, appear in the isotropic matrix [13]. As the hydrogenative polymerization reactions continues the molecules get larger and the mesophase more viscous. When the molecules reach an average molecular weight of approximately 2000 they are sufficiently large and flat to favor the formation of a liquid crystalline nematic phase called carbonaceous mesophase.

The formation of the carbonaceous mesophase follows a nucleation and growth process, typical of metastable thermodynamic systems. The droplets or spherules are easily observed because of their optical anisotropy. Attractive forces among the spherules give rise to droplet coalescence and overall growth of the mesophase. The structure of the spherules and the molecular organization of the disc-like aromatic molecules within the spherules has been described by Brooks and Taylor (1965)[14]. The characteristic mesophase mechanisms that are involved in establishing the mesophase morphology are spherule precipitation, coalescence of spherules to form a bulk mesophase, and distortion of mesophase by mechanical deformation.

As described above, the carbonaceous mesophase consists of disc-like molecules that display long range orientational order, such that the molecules lie approximately parallel to each other and there is no point-to-point registry between adjacent molecules. The orientation of each molecule is defined by its unit normal. The symmetry elements of the carbonaceous mesophase are [13]:

(a) any translation;

(b) any rotation about the unit normal to the disc-shape molecule;

(c) a rotation of $\pi$ radians about any axis parallel to the plane of the molecule.

Although the degree of symmetry is the same for a discotic nematic and a conventional rod-like nematic crystal the fact that for the discotic nematic the axis of symmetry is normal to the long dimensions of the molecule has an important consequences for optical properties, the response to mechanical stress, and the alignment in external fields such as extensional flows, electric fields, and magnetic fields [10].

## 1.3 Continuum Theory of Liquid Crystals

Liquid crystals can be continuously deformed without fracture since they are fluids. When subjected to deformation the ordered molecular orientation is affected by viscous flow torques acting on the disc-like molecules that form the liquid crystal phase. In the presence of flow, viscous flow torques perturb the equilibrium orientation, leading to spatially non-uniform non-equilibrium orientation, and creating counter-balancing orientation curvature elastic torques that generally balance the viscous torques. The non-zero elastic torques arise from a non-homogeneous orientation within the given domain, and consequently, the orientation condition at the boundary must be specified to unambiguously define a mechanical problem. A unique feature of the continuum theory of liquid crystals is that the visco-elastic torque balance must be taken into account in addition to the usual Cauchy linear momentum balance equation that holds for isotropic liquids [25]. Furthermore, the constitutive equations for the visco-elastic stress and torque components also take account of the fact that the material constants of liquid crystals are highly anisotropic. Whether liquid crystals are in static or dynamic conditions, they show very different visco-elastic responses when subjected to the same magnitude of forces with different directions. In summary, liquid crystals are anisotropic viscoelastic materials that, as shown in this thesis, behave nonlinearly even under very weak strains.

### 1.3.1 Orientational Ordering

The orientation of a disc-like molecule can be represented by a unit vector $\mathbf{u}$ normal to the disc. Disc-like molecules of a nematic liquid crystals tend to align along some common direction. Due to the centrosymmetry or the equal probabilities of between $\mathbf{u}$ and $-\mathbf{u}$, the odd moments of the orientation distribution function vanish. Thus, the second order tensor $\mathbf{M}$, representing the second order moment, becomes the leading variable to describe the orientational ordering. By its definition, $\mathbf{M}$ has the following properties [15]:

$$\mathbf{M} = \mathbf{M}^T, \quad \mathbf{M} : \delta = 1, \quad \mathbf{p} \cdot \mathbf{M} \cdot \mathbf{p} \leq 0 \tag{1.1}$$

where $\delta$ is the Kronecker delta and $\mathbf{p}$ is an arbitrary vector. A more appropriate quantity to describe the anisotropic material properties excluding the isotropic part is the second order parameter tensor $\mathbf{Q}$ given by:

$$\mathbf{Q}(\mathbf{r}) = \frac{1}{N}\sum_{i=1}^{N}(\mathbf{u}_i\mathbf{u}_i - \frac{1}{3}\delta) \tag{1.2}$$

where $N$ is the number of molecules in a small but macroscopic volume at its representative location $\mathbf{r}$. $\mathbf{Q}$ has the following properties:

$$Q_1 + Q_2 + Q_3 = 0, \quad -1 \leq 3Q_i \leq 2 \tag{1.3}$$

where $Q_i (i = 1, 2, 3)$ are the eigenvalues [15]. The number (k) of distinct eigenvalues represents different orientation states: k=1, k=2 and k=3 represent isotropic, uniaxial nematic and biaxial nematic states, respectively. Second-rank tensor material properties of liquid crystals, such as the anisotropic magnetic susceptibility, refractive indices, etc., can be described as a function of $\mathbf{Q}$ [11].

For uniaxial orientational ordering, there is one preferred orientation along a unit eigenvector $(\mathbf{n}, \mathbf{n}\cdot\mathbf{n} = 1)$ called the director. Using $\mathbf{n}$ and a single measure of alignment $(S)$, the order parameter tensor $\mathbf{Q}$ can be written as:

$$\mathbf{Q} = S(\mathbf{nn} - \frac{1}{3}\delta) \tag{1.4}$$

If we choose $\mathbf{n}$ along the $z$ axis, $\mathbf{Q}$ is given by:

$$\mathbf{Q} = S\begin{pmatrix} -\frac{1}{3} & 0 & 0 \\ 0 & -\frac{1}{3} & 0 \\ 0 & 0 & \frac{2}{3} \end{pmatrix} \tag{1.5}$$

The degree of orientational ordering, $S$, is given by [11]:

$$S = \frac{1}{2}\int f(\theta)(3\cos^2\theta - 1)d\Omega \tag{1.6}$$

where $f$ is a distribution function, $\theta$ is angle between $\mathbf{n}$ and $\mathbf{u}$, and $\Omega$ is the solid angle ($d\Omega = \sin\theta d\theta d\phi$); $f$ is independent of the azimuthal angle $\phi$ under the cylindrical symmetry about $\mathbf{n}$. For a perfect alignment along and perpendicular to $\mathbf{n}$, $S = 1$ and $S = -\frac{1}{2}$, respectively. If there is no preferred orientation as in the isotropic state, $S = 0$.

The present thesis is focused solely on uniaxial nematic liquid crystals of disc-like molecules and assumes negligible variation of $S$ so that the microstructure can be compeletly described by $\mathbf{n}$. This assumption is valid for the extensional flow considered below. In the following sections, we use Cartesian tensor notation with Einstein summation convention, and a comma followed by an index denotes partial differentiation with respect to the corresponding coordinate.

### 1.3.2 Frank Orientation Distortion Elasticity

The simplest nematic state is that of a uniform orientation domain, known as monodomain. This uniform orientation state is easily perturbed under the influence of bounding surface conditions and external fields such as shear, electric, and magnetic fields. When viewed under crossed polarizers, liquid crystals usually show iridescent textures [18]. This optical characteristics comes from the spatial variation of locally ordered average orientation $\mathbf{n}(\mathbf{r})$, giving rise to spatial variations of the anisotropic optical properties. To describe the spatial variation of orientation, Frank [16] developed a continuum theory of orientation distortion elasticity by improving on the existing theory of Oseen [17]. The distorted orientation state is described by the orientation distortion energy density $F$ given by:

$$2F = K_1(n_{k,k})^2 + K_2(\epsilon_{ijk}n_{k,j}n_i)^2 + K_3|\epsilon_{ik}n_in_{k,j}|^2 \tag{1.7}$$

where $\epsilon_{ijk}$ denotes the alternating tensor. In vector form, the above equation is:

$$2F = K_1(\nabla\cdot\mathbf{n})^2 + K_2(\mathbf{n}\cdot\nabla\times\mathbf{n})^2 + K_3(\mathbf{n}\times\nabla\times\mathbf{n})^2 \tag{1.8}$$

Here, $K_1$, $K_2$ and $K_3$, correspond to the elastic constants for the three principal modes of orientation distortion, the splay, twist and bend deformations. Figure 1-6 shows the three principal modes of orientation deformations displayed by discotic nematic liquid crystals.

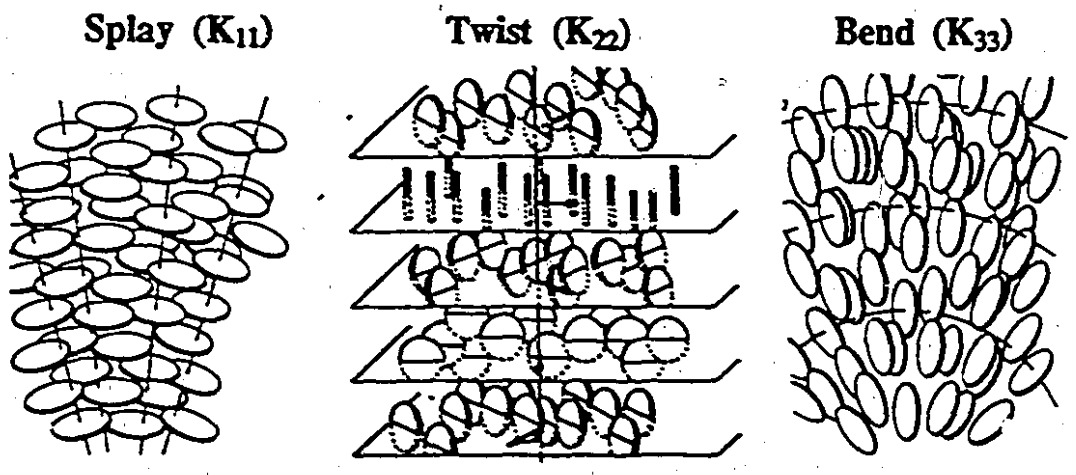


Figure 1-6: Elastic deformations of discotic nematic liquid crystals.

### 1.3.3 Leslie-Ericksen Continuum Theory

Ericksen first developed a continuum theory for viscous structured continua in which its microstructure is described by a unit vector **n**. Leslie incorporated the Frank orientation distortion elasticity to develop an anisotropic viscoelastic continuum theory of nematic liquid crystals, which turned out to be the most successful theory by far, and is usually referred to as Leslie-Ericksen (L-E) continuum theory. The governing equations used in this thesis are derived from the L-E continuum theory. The L-E equations are presented below.

#### Governing Equations and Constraints

The Cauchy linear momentum balance equation is given by:

$$\rho \dot{v}_i = \sigma_{ji,j} + f_i \tag{1.9}$$

where $\rho, v_i, \sigma_{ji}$ and $f_i$ represent the density, velocity, stress, and the body force per unit volume, and the superposed dot denotes material time derivative. The director angular momentum balance equation is given by:

$$\rho_m \ddot{n}_i = G_i + g_i + \pi_{ji,j} \tag{1.10}$$

where $\rho_m$ is the moment of inertia per unit volume, $g_i$ is the intrinsic director body force per unit volume, $G_i$ is the external director torque per unit volume and $\pi_{ji}$ is the director stress tensor.

The length of director **n** and the incompressible total mass are conserved quantities, which are expressed by the following constraints:

$$n_i n_i = 1, \quad v_{i,i} = 0 \tag{1.11}$$

**Constitutive Relations**

The constitutive relations for the stress tensor $\sigma_{ji}$, intrinsic director body force $g_i$, and the director stress tensor $\pi_{ji}$ are given by:

$$\begin{aligned} \sigma_{ji} &= -p\delta_{ji} - \frac{\partial F}{\partial n_{k,j}} n_{k,i} + \tilde{\sigma}_{ji}, \\ g_i &= \gamma n_i - \beta_j n_{i,j} - \frac{\partial F}{\partial n_i} + \tilde{g}_i, \\ \pi_{ji} &= \beta_j n_i + \frac{\partial F}{\partial n_{i,j}} \end{aligned} \tag{1.12}$$

where $\gamma$ and $\beta_i$ are Lagrangian multipliers introduced to satisfy the unit director length constraint. The dissipative contributions, $\tilde{\sigma}_{ji}$ and $\tilde{g}_i$, are given by:

$$\tilde{\sigma}_{ji} = \alpha_1 n_k n_p A_{kp} n_j n_i + \alpha_2 n_j N_i + \alpha_3 N_j n_i + \alpha_4 A_{ji} + \alpha_5 n_j n_k A_{ki} + \alpha_6 n_i n_k A_{kj}, \tag{1.13}$$

$$\tilde{g}_i = \gamma_1 N_i + \gamma_2 n_k A_{ki}, \quad \gamma_1 = \alpha_3 - \alpha_2, \quad \gamma_2 = \alpha_6 - \alpha_5 \tag{1.14}$$

where the set $\alpha_i, \quad i = 1, \ldots, 6$ is known as the Leslie viscosity coefficients. Kinematic

measures are defined by:

$$N_i = \dot{n}_i - \omega_{ik} n_k, \quad 2A_{ij} = v_{i,j} + v_{j,i}, \quad 2\omega_{ij} = v_{i,j} - v_{j,i}. \tag{1.15}$$

$N_i, A_{ij}$ and $\omega_{ij}$ are the corrotational time derivative of $\mathbf{n}$, rate of deformation tensor, and rate of rotation tensor, respectively. The Leslie viscosities are related directly to measurable quantities, the Miesowicz viscosities $(\eta_a, \eta_b, \eta_c)$ [19], the rotational viscosity $\gamma_1$, and the elongational viscosity $\nu_1$ [11] as follows:

$$\begin{aligned} 2\eta_a = \alpha_4, \quad 2\eta_b = \alpha_3 + \alpha_4 + \alpha_6, \quad 2\eta_c = -\alpha_2 + \alpha_4 + \alpha_5, \\ \gamma_1 = \alpha_3 - \alpha_2, \quad 2\nu_1 = \alpha_1 + \alpha_4 + \alpha_5 + \alpha_6. \end{aligned} \tag{1.16}$$

Usually, for discotic nematics the Miesowicz viscosity ordering is $\eta_b > \eta_a > \eta_c$ [10]. Using Onsager's reciprocal relations of irreversible thermodynamics [6], Parodi obtained the following relation [20]:

$$\alpha_2 + \alpha_3 = \alpha_6 - \alpha_5, \quad or \quad \eta_b - \eta_c = \gamma_2 \tag{1.17}$$

which reduces the number of independent Leslie viscosities from six to five.

### Visco-elastic Director Torques

Since in practical situations the inertia of the director is small [21], $\rho_m$ is assumed negligible small in equation (1.10). Then the cross product of equation (1.10) with $\mathbf{n}$ eliminates the Lagrangian multipliers $(\gamma, \beta_i)$ and yields, in the absence of external fields, the following visco-elastic torque balance:

$$0 = \epsilon_{ijk} n_j (g_k + \pi_{lk,l}) = \Gamma_i^{viscous} + \Gamma_i^{elastic} \tag{1.18}$$

The viscous torque $\Gamma^{viscous}$ and the elastic torque $\Gamma^{elastic}$ [11] acting on the director $\mathbf{n}$ are given by:

$$\Gamma_i^{viscous} = -\epsilon_{ijk} n_j (\gamma_1 N_k + \gamma_2 n_l A_l k), \quad \Gamma_i^{elastic} = -\epsilon_{ijk} n_j \left(\frac{\partial F}{\partial n_k} - \left(\frac{\partial F}{\partial n_{k,l}}\right)_{,l}\right). \tag{1.19}$$

Equation (1.18) gives the director orientation in nematic flows. Since the extensional flow is closely connected with the melt spinning of mesophase carbon fibers, it is necessary to examine the effect of such extensional flow on the director orientation.

## 1.4 Extensional Flow

Melt-spinning of carbonaceous mesophase consists of an extremely complex thermal and mechanical deformation sequence. Nevertheless as the discotic nematic liquid crystal exists the spinneret, it is subjected to a uniaxial extensional flow before solidification. The uniaxial extensional flow is the basic structuring element used in the fabrication of nearly all organic synthetic fibers, such as nylon, kevlar, and acrylic fibers. It is now widely recognized [22] that the extensional flow is the most effective deformation to promote molecular orientation that lead to the superior mechanical properties of these fibers. Thus in this thesis we also assume that the characteristic microstructural features found in the fiber cross-section arise in the section of the spinnline where the material is subjected to a uniaxial extensional flow. Figure 1-7 shows the deformations of a unit cube when submitted to a uniaxial extensional in $x$ direction. Since this extension deformation will inevitably interfere with the director orientation in discotic nematics, it is necessary to understand the effect of such flow on the director [23].

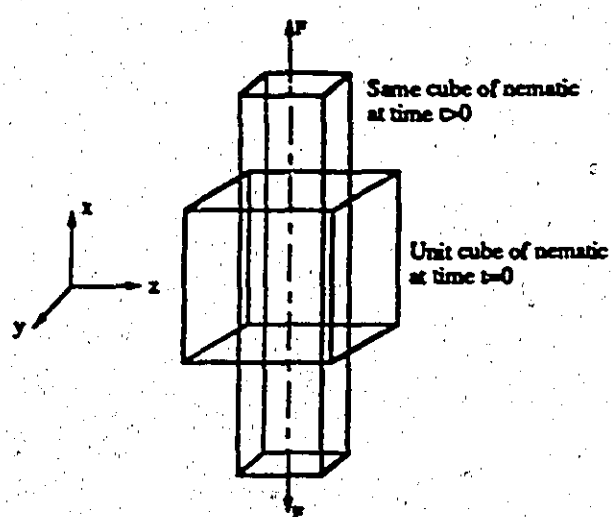


Figure 1-7: Deformation of a unit cube subjected to uniaxial extension deformations in $x$ direction

Consider the simple inelastic case ($K_1 = K_2 = K_3 = 0$), where the discotic nematic flow becomes purely viscous. The Transversely Isotropic Fluid (TIF) model of Ericksen [24] is applicable for a purely viscous nematic flow, and reads:

$$\frac{dn_i}{dt} = \omega_{ij} n_j + \lambda(A_{ij} n_j - (A_{lk} n_l n_k) n_i) \tag{1.20}$$

here $A_{ij}$ and $\omega_{ij}$ are the rate of deformation tensor and the rate of rotation tensor as defined above. $\lambda$ is the reactive number ($\lambda = -\frac{\alpha_2}{\gamma_1}$), and for discotic nematics $\lambda < 0$ [10]. According to the coordinates of Fig. 1-7, the velocity field corresponding to the uniaxial extensional start-up flow is given by [25]:

$$\begin{aligned} v_x &= \dot{\varepsilon} x H(t); \\ v_y &= -\frac{\dot{\varepsilon}}{2} y H(t); \\ v_z &= -\frac{\dot{\varepsilon}}{2} z H(t); \\ H(t) &= \left\{ \begin{array}{ll} 0 & t < 0 \\ 1 & t \geq 0 \end{array} \right\} \end{aligned} \tag{1.21}$$

where $\dot{\varepsilon}$ is the constant extension rate. The non-zero components of the corresponding deformation tensor $\mathbf{A}$ are: $A_{11} = \dot{\varepsilon}; A_{22} = A_{33} = -\frac{\dot{\varepsilon}}{2}$; this flow is irrotational and the rotational tensor $\omega_{ij} = 0$. A useful decomposition of the director field $\mathbf{n}$ and the rate of deformation tensor $\mathbf{A}$ is:

$$\begin{aligned} \mathbf{n} &= \mathbf{n}_\perp + \mathbf{n}_\parallel; \\ \mathbf{n}_\perp &= n_y \mathbf{j} + n_z \mathbf{k}; \\ \mathbf{n}_\parallel &= n_x \mathbf{i}; \\ \mathbf{A} &= \dot{\varepsilon}\delta - \frac{3\dot{\varepsilon}}{2}\mathbf{P} \end{aligned} \tag{1.22}$$

where $\delta = \mathbf{ii} + \mathbf{jj} + \mathbf{kk}$ and $\mathbf{P} = \mathbf{jj} + \mathbf{kk}$. Replacing equation (1.21) and (1.22) into equation (1.20), we obtain the following dimensionless nonlinear ordinary differential

equation:

$$\begin{aligned} \frac{d\mathbf{n}_\perp}{d\varepsilon} &= \frac{3}{2}\lambda(n_\perp^2 - 1)\mathbf{n}_\perp; \\ n_x &= sign(n_x(t=0))\sqrt{1-n_\perp^2} \end{aligned} \tag{1.23}$$

where $\varepsilon = \dot{\varepsilon}t$ is the strain. The initial conditions are: $\varepsilon = 0$; $\mathbf{n} = \mathbf{n}_0$. Integration of equation (1.23) gives the following expression for the director relaxation $\mathbf{n}(\varepsilon)$ for the uniaxial extensional start-up flow:

$$\begin{aligned} n_i(\varepsilon) &= \frac{E_{ij}n_{j0}}{|\mathbf{E}\cdot\mathbf{n}_0|}; \\ & \quad n_{j0} = n_i(0); \\ E_{ij}(\varepsilon) &= exp\{\tilde{A}_{ij}\int_0^\varepsilon \lambda d\varepsilon'; \\ & \quad \tilde{A}_{ij} = \frac{A_{ij}}{\dot{\varepsilon}} \end{aligned} \tag{1.24}$$

and in component form:

$$n_x = \frac{E_{xx}n_{x0}}{|\mathbf{E}\cdot\mathbf{n}_0|};\quad n_y = \frac{E_{yy}n_{y0}}{|\mathbf{E}\cdot\mathbf{n}_0|};\quad n_z = \frac{E_{zz}n_{z0}}{|\mathbf{E}\cdot\mathbf{n}_0|}$$

$$E_{xx} = exp(\int_0^\varepsilon \lambda d\varepsilon');\quad E_{yy} = E_{zz} = exp(-\frac{1}{2}\int_0^\varepsilon \lambda d\varepsilon'); E_{ij} = 0\ for\ i \neq j \tag{1.25}$$

where $n_{j0}$ is the $j$th component of the initial director orientation $\mathbf{n}(0)$. Since $\lambda$ is a constant, the above equation can be written as:

$$E_{xx} = e^{\lambda\varepsilon}; E_{yy} = E_{zz} = e^{-\frac{\lambda\varepsilon}{2}}; E_{ij} = 0\ for\ i \neq j \tag{1.26}$$

here $\varepsilon = \dot{\varepsilon}$ is the strain and $\dot{\varepsilon}$ is the extension rate. It is clear from equation (1.26) that since $\lambda < 0$ for discotic nematics, the $x$ component of the director $\mathbf{n}$ will decrease exponentially with time while the $y$ and $z$ components of $\mathbf{n}$ will increase. Therefore the relaxation of the director $\mathbf{n}$ under extension, as in the melt spinning flow of carbonaceous mesophases, will restrict $\mathbf{n}$ within the plane normal to the fiber axis, which is exactly the cross-section of the fiber. Thus we are led to the following significant conclusions: 1)

extensional viscous torques orient the director anywhere on the plane perpendicular to the extension axis; 2) any cross-sectional microstructure formation in cylindrical fibers subjected to extensional flow must arise due to the elastic torques (see equation (1.19)).

## 1.5 Thesis Scope

This thesis is devoted to simulation of the pattern formation of melt spun mesophase carbon fibers. The mesophase carbon fibers is approximated by a monodisperse uniaxial discotic nematic liquid crystal [12]; the melt spinning flow is approximated by a steady, isothermal, incompressible, uniaxial extensional flow [25]. Using cylindrical coordinates $(r, \theta, z)$, the fiber is approximated by the cavity between two concentric cylinders with the $z$ direction coincides with the fiber axis. The outer cylinder represents the surface of the fiber, and the inner cylinder represents the isotropic core along the fiber axis. From the results of the analysis on extensional flow presented above, the director $\mathbf{n}$ is restricted to the transverse plane of the fiber. The main parameters considered in this thesis are the Frank elastic constants $K_1$ and $K_3$, which represent the splay and bend deformations of the director orientation. Both fixed and unrestrained surface orientation of the director are considered in this study. Emphasis is placed on the multiple solutions of the director field $\mathbf{n}(r, \theta)$ when varying the elastic anisotropy conditions due to the changes in the ratio of $K_1$ and $K_3$.

## 1.6 Thesis Objectives

The main objectives of this thesis are: 1) to reproduce planar textures observed in carbon fibers through numerical simulations based on well-established theories about discotic nematic liquid crystal materials, 2) to provide a comprehensive characterization of planar orientation patterns of discotic nematics liquid crystals subjected to extensional flow, 3) to identify the pattern selection mechanism in melt spinning process of mesophase carbon fibers.

The thesis objectives are directly motivated by actual microstructural phenomena

commonly observed during the fabrication of carbonaceous mesophase fibers, as shown in Fig. 1-2, 1-3, and 1-4.

## 1.7 Thesis Organization

This thesis is organized as follows:

Chapter 1 presented the necessary background concepts on the discotic nematic liquid crystalline materials, including some preliminary analysis on the effect of melt spinning flow on director orientation.

Chapter 2 presents the simulation and analysis of the pattern formation in fiber spinning that explains the planar oscillatory textures observed in the transverse plane of mesophase carbon fibers (Fig. 1-2). An analysis on the stability of the numerically obtained director orientation is also included. The main effects of elastic anisotropy on the pattern selection are shown using computational bifurcation methods.

Chapter 3 presents simulation and analysis of the effect of temperature on the pattern formation in mesophase carbon fibers. The various transverse patterns, shown in Fig. 1-3 and 1-4, in different temperature ranges are reproduced and explained using time-dependent numerical simulations.

Chapter 4 presents a summary of this thesis, including conclusions and contributions to existing theories on pattern formation in carbon fibers.

# Bibliography


[1] Pebbles L.H.Jr., International Materials Review, **39**, 75(1994).

[2] Pebbles L.H.Jr., *Carbon Fibers-Formation, Structure, and Properties*, (CRC Press, Boca Raton, 1995).

[3] Singer L.S., *Ind. Conv. of Coal and Carbon to Gas, Liquid, and Solid Products*, (London, 1981).

[4] Honda H., Mol. Cryst. Liq. Cryst.,**94**, 97(1983).

[5] Singer L.S., Fuel, **60**, 839(1981).

[6] Fatholahi B. and White J.L., J. Rheol., **38**, 1591(1994).

[7] Pencock G.M., Taylor G.H. and FitzGerald J.D., Carbon, **31**, 591(1993).

[8] Matsumoto T., Pure Appl. Chem. **57**, 1553(1985).

[9] Otani S. and Oya A., *Petroleum Derived Carbons*, ACS Symp. Ser. No. 303, American Chemical Society, Washington D.C., 322(1986).

[10] Ho A.S.K. and Rey A.D., Rheol. Acta., **30**, 77(1991).

[11] de Gennes P.G. and Prost J., *The Physics of Liquid Crystals*, 2nd ed. (Clarendo, Oxford, 1993).

[12] Chandrasekhar S., *Liquid Crystals*, 2nd ed. (Cambridge Press, 1992).

[13] Zimmer J.E., White J.L., In *Advances in Liquid Crystals*, Vol. 15, Academic Press, 157(1982).

[14] Brooks J.D., Taylor G.H., Carbon, **3**, 185(1965).

[15] Ericksen J.L., Arch. Rat. Mech. Anal., **113**, 97(1991).

[16] Frank F.C., Discuss. Faraday Soc. **25**, 19(1958).

[17] Oseen C.W., Ark. Mat. Astr. Fys. A, **19**, 1(1925).

[18] Collings P.J., *Liquid Crystals: Nature's Delicate Phase of Matter*, (Princeton Univ. Press, Princeton, 1990).

[19] Miesowicz M., Nature, **158**, 27(1946).

[20] Parodi O., J. Physique, **31**, 581 (1970).

[21] Saupe A., Mol. Cryst. Liq. Cryst., **7**, 59(1969).

[22] Ziabicki A. and Kawai H., *High Speed Fiber Spinning*, (John Wiley & Sons, New York, 1985).

[23] Singh A.P. and Rey A.D., J. Phys. II France, 4, 645(1994).

[24] Ericksen J.L., Koll. Zeit., **173**, 117(1960).

[25] Bird R.B., Curtiss C.F., Armstrong R.G. and Hasager O., *Dynamics of Polymeric Liquids* (Wiley, New York, 1987).

# Chapter 2

# Pattern formation and nonlinear phenomena in streched discotic liquid crystal fibers

## 2.1 Summary

This chapter presents a nonlinear numerical and bifurcation analysis of pattern formation phenomena in discotic nematic liquid crystal confined to annular cylindrical cavities and subjected to extensional deformations. The results are of direct relevance to understanding the industrial melt spinning of mesophase carbon fibers, using discotic nematic liquid crystals precursor materials . Three types of orientation patterns are identified in this study: spatially constant (radial), monotonic (pinwheel), and oscillatory (zig-zag). Numerical and closed form analytical results predicting continuous transformations between the radial, pinwheel, and zig-zag radial orientation modes are presented. The bifurcation analysis provides a direct characterization of the parametric dependence and the transitions between these three basic patterns, and provides a complete understanding of the multistability phenomena that is present in the oscillatory orientation patterns. In general it is found that small fibers of nearly elastically isotropic discotic nematic liquid crystals tend to adopt the classical ideal radial texture, while larger fibers with

anisotropic elastic moduli tend to yield the zig-zag texture. Fixed arbitrary surface orientation of intermediate size and anisotropy tend to adopt the pinwheel texture. The theoretical results are able to explain the main features and mechanisms that lead to the commonly observed cross-section textures of industrially spun mesophase carbon fibers.

## 2.2 Introduction

The industrial fabrication of mesophase carbon fibers [1-3] is based on the melt spinning of discotic nematic liquid crystals into micron-sized cylindrical filaments. As in other man-made organic fibers molecular orientation is a key parameter that dominates the mechanical property profile. For disk-like molecules the distinguishing molecular direction is the unit normal to the molecular disks, and the average orientation characteristic of nematic ordering arises from the close alignment of the molecular unit normals. During fiber spinning, a uniaxial extensional stretching flow orients the longest molecular dimension of the disk-like molecules close to the extension (flow direction), such that the average molecular orientation is normal to this direction, and contained in the plane normal to the fiber axis. Thus any spun mesophase fiber cross-section displays a planar orientation. A variety of planar orientation patterns have been frequently reported in the literature, including the onion, radial, and zig-zag radial patterns, shown in Fig.1 [4]. The shown patterns contain a line defect along the fiber axis, while the surface orientation is planar for the onion pattern, homeotropic for the radial, and arbitrary for the zig-zag. It should be noted that in actual fibers the defect gives rise to a macroscopic isotropic core, apparently much larger than the typical molecular size of nematic disclinations [5]. The radial zig-zag pattern observed in actual fibers [6] has a position dependent amplitude and wave-length but the basic textural feature of interest is the radially oscillatory trajectories of the molecular planes.

The selection mechanisms that drive the pattern formation in mesophase fibers spun from discotic nematic liquid crystals are at present not well understood, but due to strong structure-properties correlations they are essential for product optimization. On the other hand, the closely related problem of pattern formation in cylindrical cavities filled with

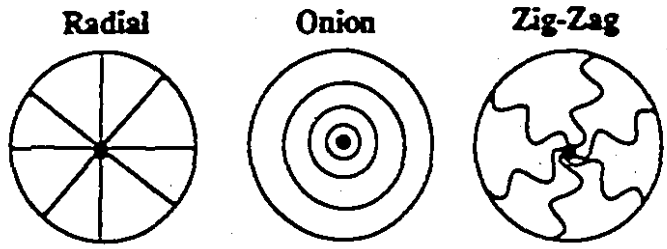


Figure 2-1: Schematic representation of the molecular trajectories in the cross-section of mesophase fibres observed during industrial spinning process (Peebles, Pencock et al.).

rod-like nematics is better understood [7, 8]. In the latter case, theoretical predictions using energy minimizing models, are able to reproduce many observed patterns. Below we show that similar elastic minimization mechanisms are able to explain the pattern formation phenomena in discotic nematic filaments subjected to ideal extensional flows.

Previous work [9] on pattern formation in confined discotic nematic liquid crystals mainly focused on predictions of the radial and radial zig-zag patterns, using a simplified linear analysis. The analysis predicted that oscillatory pattern arises due to the anisotropy that characterizes the planar elastic deformation modes, but only if the outer boundary conditions are not homeotropic. Thus the only transformation leading to a zig-zag pattern involves a bifurcation of the pinwheel pattern, also known as the magic spiral [5], in which the molecular trajectories follow a pinwheel pattern (see Fig.4). This is obviously in disagreement with experiments [6], where the surface orientation can be arbitrary and in fact it is ill-defined [6]. In addition, the linear analysis of [9] is only valid for small director distortions, and it also predicts unbounded oscillations for certain critical values of the fiber radius, which is again unphysical. The above shortcomings indicate an incomplete knowledge of what parameter envelopes lead to specific patterns in stretched discotic nematic liquid crystal filaments. To develop a complete picture of pattern formation in confined discotic nematic liquid crystals here we focus on orientation patterns that arise from all possible continuous transformations of the ideal radial pattern, in which the molecular discs follow radial trajectories (see Fig. 4). In addition since the isotropic cores found along the fiber axis are in practice of macroscopic size, we study confinement in an annular geometry [6].

For rod-like liquid crystals, previous work on planar textures of confined nematics in cylindrical cavities [10] proved the existence of spatially oscillatory solutions to the equilibrium equation, and also established the stability properties of the solutions. In [10] it is predicted the existence of an infinite number of oscillatory solutions for homeotropic boundary conditions when the two relevant splay-bend elastic constants are different, which in general disagrees with the multiple bifurcation and multistability phenomena in cylindrical confined geometries as shown below. Analysis of the linearized model for confined rod-like nematics in cylindrical cavities [11] shows oscillatory solutions for non-homeotropic boundary conditions. However, due to the shortcomings of linearization, the bifurcation and multistability phenomena, due to non-linearity of the elastic free energy model, remained unexplored. In this chapter, we overcome the above mentioned shortcomings of previous works and give a complete analysis of planar textures of confined nematics in cylindrical cavities. Non-planar pattern formation as well as planar pattern formation with off-axis singularities in rod-like nematics confined to cylindrical cavities have also been charracterized using energy minimization model [12]. Nevertheless these works do not consider the planar patterns studied here.

The objective of this chapter is: 1) to reproduce and explain the main pattern formation phenomena that are observed during the spinning of carbonaceous mesophase using well established liquid crystal elasticity models, 2) to provide a comprehensive characterization of planar orientation patterns of discotic nematics liquid crystals subjected to extensional flow, and 3) to establish the main bifurcational and non-linear phenomena present in discotic nematics in cylindrical cavities.

This chapter is organized as follows. Section 3 deals with the elastic modes of discotic nematics, and discusses the elastic anisotropies in planar orientation patterns. Section 4 presents the mathematical model that describes steady state planar orientation patterns in cylindrical cavities in the presence of fixed boundary conditions. Equations that validate the planarity assumption in the presence of extensional (fiber spinning) flow are presented. Section 5 presents the numerical results and discussion. The results are organized and classified along the values of the governing parameters. Closed form bifurcation thresholds, bifurcation diagrams, and stability diagrams are presented. A summary of

the main features of the pattern formation phenomena is also included.

## 2.3 Elastic Modes of Discotic Nematics Liquid Crystals

In this section we describe the main features of nematic elasticity for discotic nematics in cylindrical cavities displaying planar (2D) textures, and use them to identify the elastic modes in typical mesophase carbon fiber textures. Figure 2-2 shows the molecular geometry, positional disorder, and uniaxial orientational order of the model uniaxial discotic nematic liquid crystal considered in this chapter [5]. The partial orientational ordering of the molecular unit normals $\mathbf{u}$ is along the average orientation or director $\mathbf{n}$ ($\mathbf{n} \cdot \mathbf{n} = 1$), and differs from that of rodlike molecules in that $\mathbf{u}$ is along the shortest molecular dimension. This geometric difference is the source of the reversal in the ordering of viscoelastic [13, 14] as well as other properties [2], that arise when comparing disk-like and rod-like uniaxial nematics. This chapter is restricted to the study of planar patterns, containing splay and bend deformations [5]. Figure 2-3 shows the splay mode of modulus $K_1$, and the bend mode of modulus $K_3$. Note that in contrast to rod-like nematics, for disk-like nematics the bending disk's trajectories give rise to splay deformation (left figure), and the splaying disk's trajectories give rise to bend deformation (right figure); by disk trajectory we mean the curve locally orthogonal to the director. Using a circular cylindrical coordinate system $(r, \psi, z)$, the $z$-coordinate is along the fiber axis, and the transverse plane is spanned by the azimuthal direction of ($\psi$) and the radial ($r$) direction; here $0 \leq \psi \leq 2\pi$ and $r_c \leq r \leq r_o$, where $r_c$ is the isotropic core radius, and $r_o$ is the outer radius which for typical mesophase carbon fibers is in the micron size range. In this cylindrical geometry, the stationary radially dependent planar director field of Fig.1 can be parametrized as $\mathbf{n}(r) = (n_r, n_\psi, n_z) = (\cos\theta, \sin\theta, 0)$; here $n_z = 0$ means planar orientation and absence of twist deformations [5]. Figure 2-4 shows schematics of a radial transverse texture (left) and a radial zig-zag texture(right), typically observed in mesophase carbon fibers [4, 6]. The full lines indicate the disk's trajectories, which are

locally orthogonal to the directors. Based on our previous discussion, it follows that the radial texture of a uniaxial discotic nematic, defined by $n_\psi(r) = 1$ and $r_c \leq r \leq r_o$, contains a pure bend mode. On the other hand, a radial zig-zag texture consists of a mixed splay-bend deformation mode, and in addition $n_\psi(1) \neq 1$. A comparison of the two schematics shown in Fig. 2-4 indicates that if the radial zig-zag texture is selected over the pure radial texture then the trade-off of bend by splay in the oscillatory pattern must be energetically favorable, as quantitatively shown below.

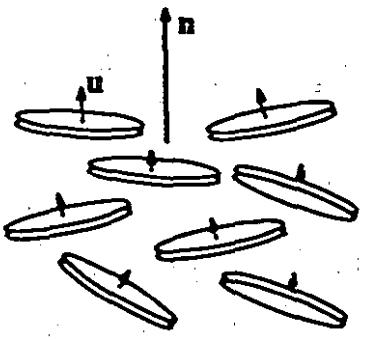


Figure 2-2: Orientational ordering in the uniaxial discotic nematic phase. The molecular normals **u** of the randomly positioned disklike molecules, partially orient along the director **n**.

For low molecular mass discotic nematics, theory [13] and experiment [15] show that $K_1 > K_3$. An increase in the molecular weight of disk-like nematics, just as for rod-like nematics [16], can be expected to reverse the ordering of the elastic constants, so that for higher molecular weight discotic nematics, like carbonaceous mesophases, we can expect $K_3 > K_1$. Thus, just as polymeric rods avoid the splay of the radial texture by introducing director oscillations [10, 11], polymeric disks avoid the bend of the radial texture by a zig-zagging director field [9].

## 2.4 Governing Equations

To establish the origin of planar orientation textures we first discuss the effect of an external extensional flow in the $z$-direction on the texture formation in the $\psi - r$ plane.

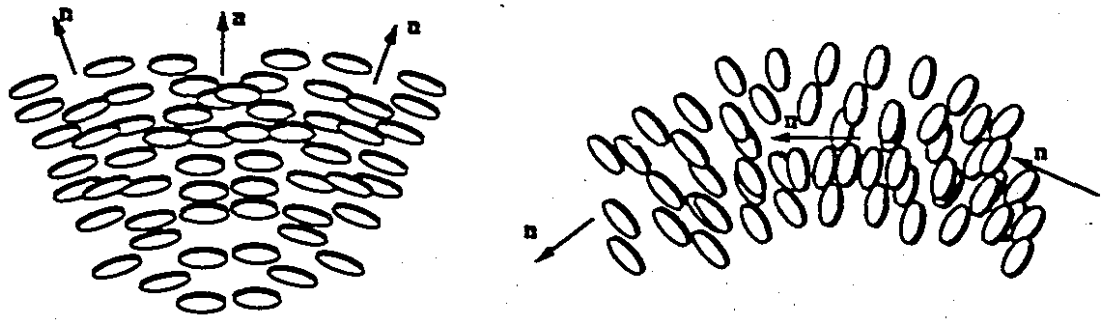


Figure 2-3: Schematics of the elastic splay deformation (left) and bend deformation (right) for uniaxial discotic nematics. Note that the splay (bend) mode involves bending (splaying) of the disk's trajectories, in contrast to the case of uniaxial rod-like nematics. A disk trajectory is a curve locally orthogonal to the director.

The non-zero components of the rate of deformation tensor $A_{ij}$ for an extensional flow are [17]: $A_{zz} = -A_{rr} = \dot{\varepsilon}$, where $\dot{\varepsilon}$ is the extension rate, and the vorticity tensor for this irrotational flow is $\mathbf{W} = \mathbf{0}$. At steady state, the viscous torques $\mathbf{\Gamma}^v$ acting on the director are $\mathbf{\Gamma}^v = -\mathbf{n} \times (\gamma_2 \mathbf{A} \cdot \mathbf{n})$, where the $\gamma_2$ is a torque coefficient [5]. As is well known [18], in this flow the stable director orientation is normal to the extension direction (i.e. transverse $\psi - r$ plane), and therefore $\mathbf{\Gamma}^v = 0$. Thus the net effect of the extensional flow on the texture formation is to keep the director in the $\psi - r$ transverse plane. Therefore, we may conclude that, given sufficient long process times as compared to reorientation times, the transverse radial zig-zag pattern is selected by the minimization of the splay-bend elastic free energy per unit fiber length. If the inequality in the time scales does not hold the assumption of planarity does not generally hold. In actual typical fiber spinning process there is ample evidence that shows that the process time is greater than the director reorientation time, so that the planar orientation assumption is realistic, and always observed [4, 6].

Since the viscous torques $\mathbf{\Gamma}^v$ due to the extensional flow acting on the director $\mathbf{n}$ vanish with planar orientation ($n_z = 0$), the selection of the pattern is just dictated by a minimization of the Frank [5] elastic energy due to, at most, splay and bend modes.

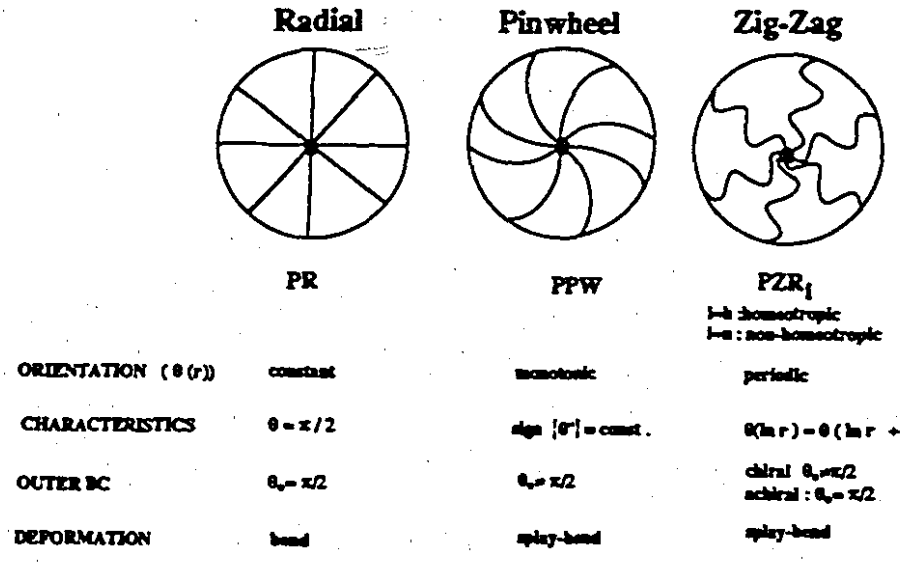


Figure 2-4: Schematics of a planar radial pattern (PR), the planar pinwheel pattern (PPW), and the planar zig-zag radial pattern (PZRi; i=h: homeotropic, i=n: non-homeotropic). The text below the schematics summarizes the main features of each pattern.

The equilibrium equation for the director of discotic nematic liquid crystals is derived from the extremum condition of the free energy. Since there are no twist deformations in planar orientation, the Frank elastic energy density reduces to [5]:

$$f = \frac{1}{2}\{K_1(\nabla \cdot \mathbf{n})^2 + K_3(\mathbf{n} \times \nabla \times \mathbf{n})^2\} \tag{2.1}$$

here $\mathbf{n}$ is the director. Note that saddle-splay elasticity ($K_{12}$) plays no role in planar patterns. Thus the total free energy is given by:

$$F = \int_\Omega f dv \tag{2.2}$$

where $\Omega$ is the total volume. Expressing the director $\mathbf{n}$ in terms of independent variables $q_i$, and taking the first variation of the total free energy integral, we obtain the Euler-Lagrange equilibrium equation:

$$\frac{\delta F}{\delta \mathbf{n}} = \frac{\partial f}{\partial \mathbf{n}} - \nabla \cdot \frac{\partial f}{\partial \mathbf{n}'} = 0 \tag{2.3}$$

where the $\nabla = \frac{\partial}{\partial q_i}$ and $\mathbf{n}' = \frac{\partial \mathbf{n}}{\partial q_i}$. We assume that the pattern is rotationally symmetric in the cross-section $\psi - r$ plane, such that the director $\mathbf{n}$ would be only a function of the radial distance ($r$) from the axis of rotational symmetry. The total free energy is:

$$F = \int_L F_{2d} dr \tag{2.4}$$

where

$$F_{2d} = 2\pi \int_{R_c}^{R_o} f r dr = 2\pi \int_{u_c}^{u_o} f\left(\mathbf{n}, \frac{d\mathbf{n}}{du}, u\right) du. \tag{2.5}$$

is the free energy per unit length, and $u = ln\left(\frac{r}{r_c}\right)$. Equation (2.4) and (2.5) show that the numerical value of the total free energy per unit length depends on $f$. In polar coordinates, the director $\mathbf{n}$ is expressed by the polar angle $\phi$ as:

$$\mathbf{n}(\phi) = (\cos\phi, \sin\phi, 0) \tag{2.6}$$

where $\phi$ is position dependent, $\phi = \phi(u)$, and the unit length restriction $\mathbf{n} \cdot \mathbf{n} = 1$ is satisfied. In terms of the generalized variable $u$, the equilibrium equation becomes

$$\frac{\partial f}{\partial \phi} - \frac{d}{du}\frac{\partial f}{\partial \phi'} = 0 \tag{2.7}$$

where the prime denotes differentiation with respect to $u$. This is the governing equation in this analysis. Using the expression of $\mathbf{n}$ of (2.6) in (2.3), we have

$$\begin{aligned} f = & \frac{K_1}{2} \{\cos^2\phi - 2\phi' \sin\phi\cos\phi + \phi'^2 \sin^2\phi\} \\ + & \frac{K_3}{2} \{\sin^2\phi + 2\phi' \sin\phi\cos\phi + \phi'^2 \cos^2\phi\} \end{aligned} \tag{2.8}$$

Taking the variation of above expression of the free energy density, we obtain the equilibrium equation,

$$\begin{aligned} \sin\phi\cos\phi\{-K_1 + K_3\} + \sin\phi\cos\phi\{-K_1 + K_3\}\phi'^2 \\ + \{-K_1 \sin^2\phi - K_3 \cos^2\phi\}\phi'' = 0 \end{aligned} \tag{2.9}$$

Scaling with $K_3$ we get:

$$\sin\phi\cos\phi\{(1-\mu)(1+\phi'^2)\} - \{\cos^2\phi + \mu\sin^2\phi\}\phi'' = 0 \tag{2.10}$$

here $\mu = \frac{K_1}{K_3}$. The boundary conditions studied here are:

$$\begin{aligned} u(0) &= \frac{\pi}{2} \\ u(u_o) &= \phi_o \end{aligned} \tag{2.11}$$

The solution to (2.10, 11) is $\phi(u)$ and the parameter vector is $p = (\mu, \phi(u_o), \Delta u)$. The deviation of $\mu$ from 1 denotes elastic anisotropy, the deviation of $\phi(u_o)$ from $\phi(0)$ introduces asymmetric boundary conditions, and $\Delta u$ is a scale of fiber size such that increasing (decreasing) $\Delta u$ represents smaller (larger) fiber cavities.

The equilibrium equation (2.10) is a nonlinear second order ordinary differential equation. For symmetric boundary conditions of $\phi(0) = \phi(u_o) = \frac{\pi}{2}$ ($\phi(0) = \phi(u_o) = 0$), the trivial solutions of $\phi = \frac{\pi}{2}$ ($\phi = 0$) exists for all values of $\mu$. For asymmetric boundary conditions, i.e. $\phi(0) \neq \phi(1)$, previous work [9] has shown the existence of oscillatory solutions when the elastic constants are not equal ($\mu \neq 1$), using a linearized equilibrium equation. Here we complete this work, by carrying out a full analysis of the nonlinear equation (2.10).

Given the possibility of multistability and solution multiplicities, generic in nonlinear equations, we compute all equilibrium points of equation (2.9) using an efficient root finder based on the shooting method [19]. Briefly, we rewrite the governing equation (2.10) as two first order differential equations system:

$$\begin{aligned} \phi' &= \psi \\ \psi' &= \frac{(-\mu+1)\sin\phi\cos\phi(1+\psi^2)}{\mu\sin^2\phi + \cos^2\phi} \end{aligned} \tag{2.12}$$

The boundary conditions are:

$$\phi(0) = \frac{\pi}{2}$$

$$\psi(0) = p \tag{2.13}$$

where $p = \phi'(0)$ is a new parameter. By introducing the new parameter $p$, we consider the value of $\phi(u_o)$ as a function of $p$, once $\mu$ is fixed. We next perform a numerical study using a fourth order Ronge-Kutta method [19]. By solving for $p$ for a given value of $\phi(u_o)$, we are able to find all the stable as well as unstable solutions of equation (2.10). The numerical study identified all the solution branches and their parametric dependencies on the outer boundary condition $\phi(u_o)$, and elastic anisotropy $\mu$, for a given value of $u_o$.

## 2.5 Numerical Results and Discussions

The numerical solutions found in this study are naturally classified and characterized by the symmetry properties of the director field. Figure 2-4 summarizes the classifications of the three classes of planar patterns arising in discotic nematics in annular cylindrical cavities with surface orientation at the inner radius fixed at $\frac{\pi}{2}$. Below each descriptive name (radial, pinwheel, zig-zag) we show a sketch of the orientation profiles, and the main signatures of each pattern. The planar radial (PR) pattern has a pure bend deformation and the outer boundary condition is homeotropic ($\phi(u_o) = \frac{\pi}{2}$). The planar pinwheel (PPW) pattern, also known as the magic spiral [5], has monotonic splay-bend deformations, and arise with non-homeotropic ($\phi(u_o) \neq \frac{\pi}{2}$) boundary conditions. The planar zig-zag radial (PZRi) pattern has periodic splay-bend deformations and may occur with homeotropic (i=h) or non-homeotropic (i=n) outer boundary conditions. Figure 2-5 shows a block diagram that summarizes the transformation paths between the three orientation patterns. The figure shows that the radial pattern can be transformed into the pinwheel pattern by changing the outer surface orientation ($T_1$). The radial pattern can also be transformed into the homeotropic zig-zag radial pattern (PZRh) by temperature changes (increase in elastic anisotropy) or by increasing the ratio between the outer and the inner radius ($\Delta u$). Similarly, the pinwheel (PPW) pattern can be transformed into a non-homeotropic zig-zag radial pattern (PZRn) by the change in temperature and by increasing $\Delta u$. The transformation between homeotropic and non-homeotropic patterns

are achieved by changing the outer surface orientations.

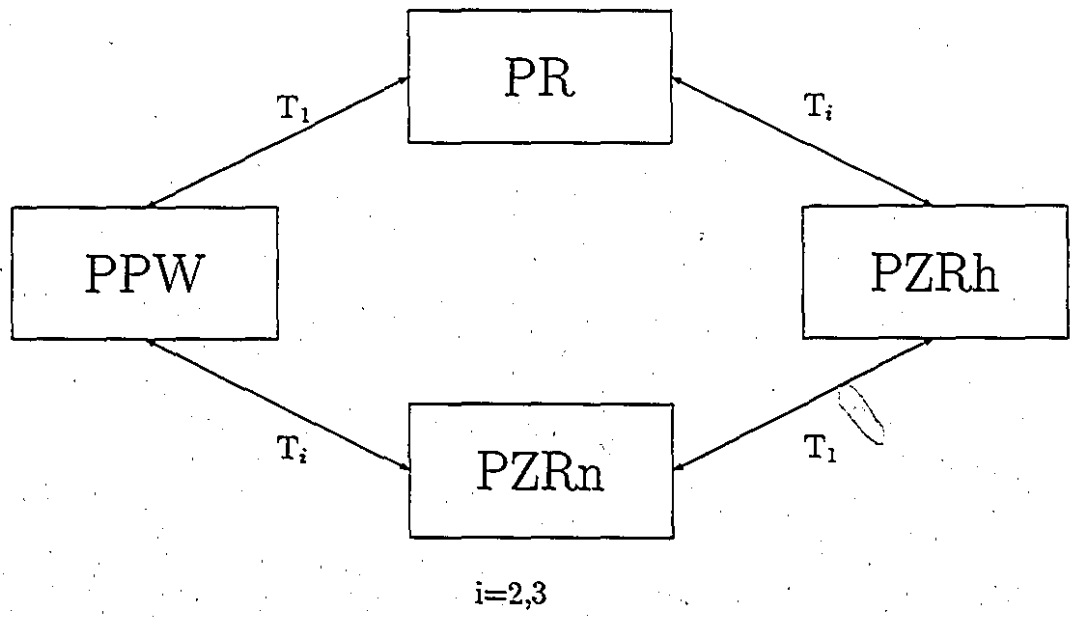


Figure 2-5: Block diagram of the transformation paths between planar radial (PR), planar pinwheel (PPW), and planar zig-zag radial (PZR) patterns. $T_1$ corresponds to surface orientation change, $T_2$ corresponds to temperature change, and $T_3$ to fiber radius change.

Figure 2-6 shows a summary of numerical simulation results of the orientation $\phi(rad.)$ as a function of dimensionless distance $u$, for $\Delta u = 1$. These results summarize the $T_1$ and $T_2$ transformations. Starting from the top left, the panels towards the right correspond to increasing elastic anisotropy ($\mu = \frac{K_1}{K_3}$) and the panels towards the bottom correspond to increasing values of outer cylinder surface orientation ($\phi(u_o)$). The orientation changes in the different panels of the figure clearly reflect the transformation

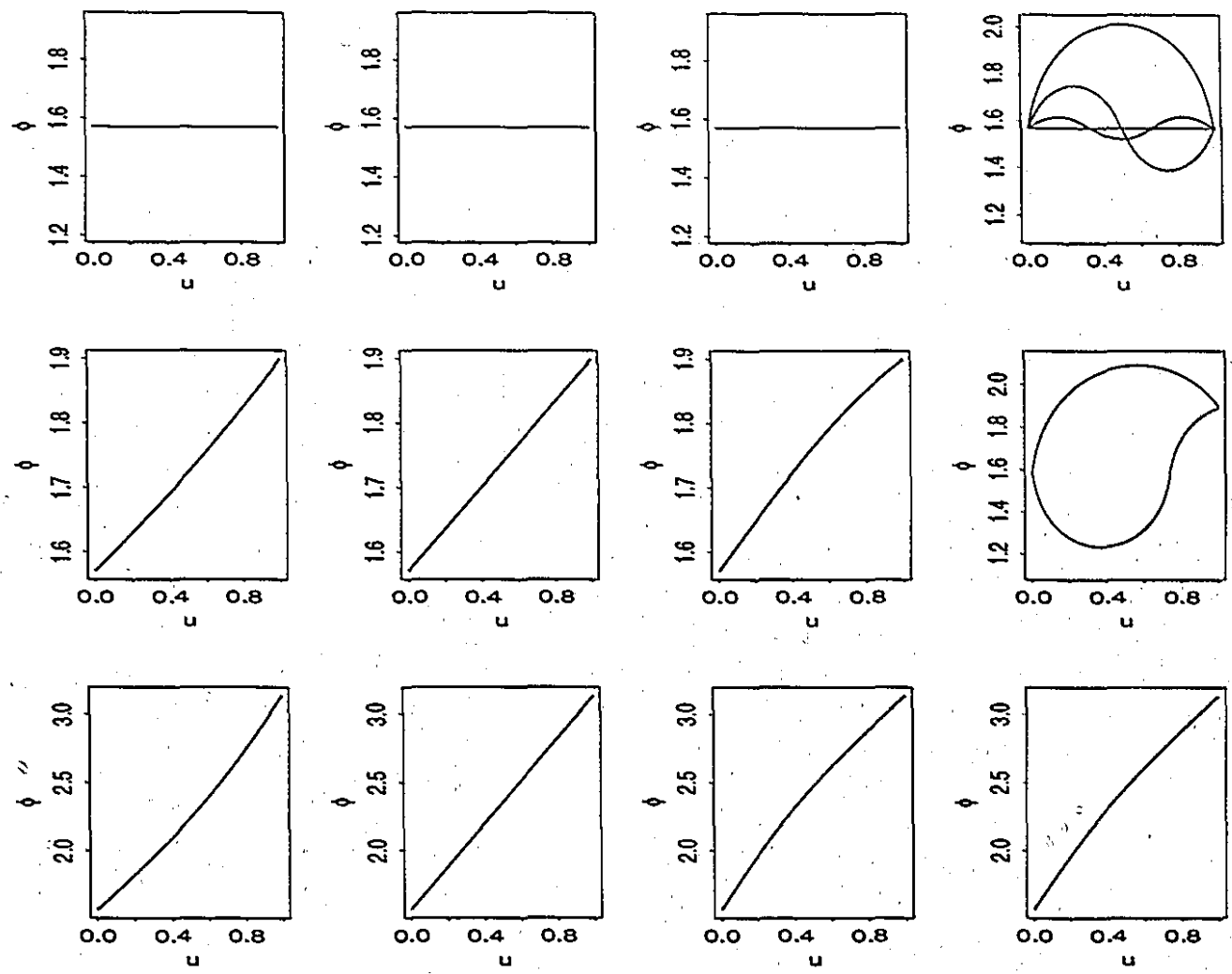


Figure 2-6: Summary of representative solutions to equation (2.9) for $\Delta u = 1$, and different parametric conditions. Symmetric boundary conditions (top row), asymmetric boundary conditions of $\phi(1) = 1.9(rad)$ (middle row) and asymmetric boundary conditions of $\phi(1) = \pi$ (bottom row). For elastic anisotropy, $\mu > 1$ (left column), $\mu = 1$ (left middle column), $1 > \mu > \mu_{c,1}$ (right middle column), and $\mu < \mu_{c,1}$ (right column).

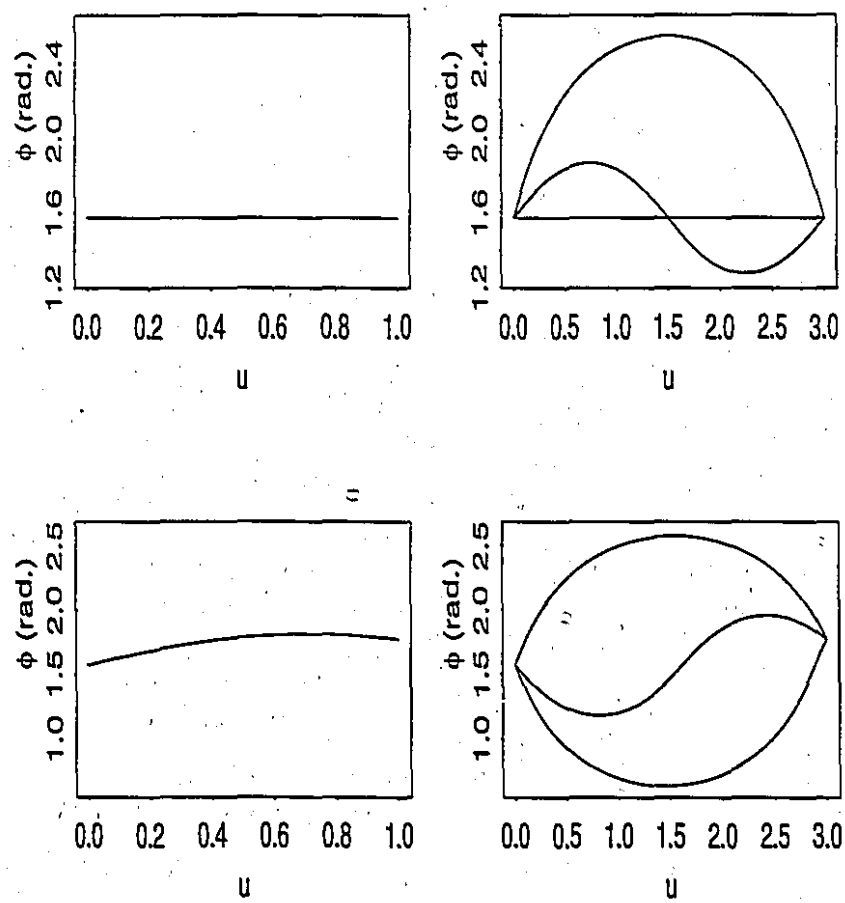


Figure 2-7: Summary of representative solutions to equation (2.9) for $\Delta u = 1$ (left column) and $\Delta u = 3$ (right column), for different outer boundary orientation, $\phi(u_o) = \frac{\pi}{2}$ (upper row) and $\phi(u_o) = 1.77(rad)$ (lower row). Here $\mu = 0.15$ is fixed for all cases.

paths shown in Fig. 2-5. Moving towards the left in the top row corresponds to the $T_2$ transformation of the radial pattern (PR) into the homeotropic zig-zag radial pattern (PZRh). Moving towards the left in the middle and the bottom rows correspond to the $T_2$ transformation paths of planar pinwheel pattern (PPW) into non-homeotropic zig-zag radial pattern (PZRn). Moving down corresponds to the $T_1$ transformation between (PR) and (PPW) patterns(left column), and also the $T_1$ transformation between (PZRh) and (PZRn) patterns (right column).

Figure 2-7 shows the corresponding summary of the $T_1$ and $T_3$ transformations. In Fig. 2-7 the elastic anisotropy is fixed at $\mu = 0.15$, and left column represent the patterns for $\Delta u = 1$, while the right column represents the patterns for $\Delta u = 3$. Moving from top to bottom in the left column corresponds to the $T_1$ transformation between (PR) and (PPW) pattern, and moving vertically on the right column corresponds to the $T_1$ transformation between (PZRh) and (PZRn) pattern. Moving on the top row corresponds to the transformation $T_3$ between (PR) and (PZRh) patterns. Moving along the bottom row corresponds to the transformation $T_3$ between (PPW) and (PZRn) patterns.

### 2.5.1 Solutions with symmetric boundary conditions

With symmetric homeotropic boundary condition of $\phi(0) = \phi(1) = \frac{\pi}{2}$, the radial (PR) solution ($\phi = \frac{\pi}{2}$) exists for all $\mu$, as shown in the previous section. For $\mu > 1$, $\mu = 1$ and $1 > \mu > \mu_c$, the trivial solution is the unique solution of the equation, where $\mu_c$ denotes a critical value of elastic anisotropy. The stability of the radial solution will be discussed later in this section.

Multiple oscillatory solutions, representing the homeotropic zig-zag radial pattern (PZRh) are found when the ratio exceeds a certain value of $\mu_c$. For $\Delta u = 1$, we found the critical value of $\mu_c = 0.092$.

Figure 2-8 shows a section of the bifurcation diagram, presented as the orientation amplitude ($\max|\phi|$) as a function of the elastic anisotropy of $\mu$. The horizontal (zero amplitude) line represents the radial (PR) solution and the five curves represent members of the PZRh family. The first bifurcation branch A represents an oscillatory solution with half-wavelength. The bifurcation occurs at $\mu = 0.092$, and the amplitude of the

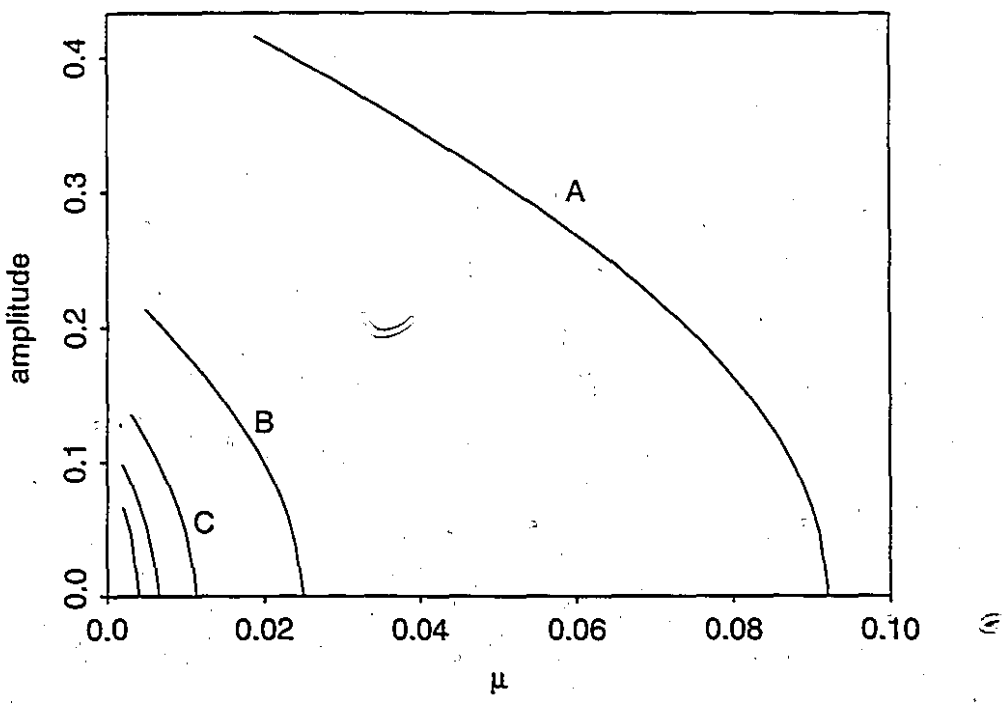


Figure 2-8: Bifurcation diagram. Amplitude of oscillatory solutions as a function of the elastic anisotropy $\mu$, for $\Delta u = 1$ and $\phi(1) = \frac{\pi}{2}$. It shows multiple solution branching and finite amplitude growth as $\mu$ decreases. The horizontal line corresponds to the ideal radial (PR) texture, while the bifurcation branches correspond to the oscillatory zig-zag radial (PZRh) texture. For $\mu < 0.092$ the PR solution is unstable. For $\mu < 0.028$ there are multiple oscillatory solutions.

solution grows as $\mu$ decreases. At $\mu = 0.025$, the system bifurcates again and generates a new oscillatory solution branch B with one full wavelength. As $\mu$ decreases further, more branches are generated, representing solutions with one-half-wavelength C, two-wavelength, two-half-wavelength and so on. Figure 2-8 clearly shows the strong non-linear features of the model, with typical multiple bifurcations of the spatially constant solution (PR) into a family of spatially oscillatory solutions (PZRh) at critical values of elastic anisotropy ratio $\mu_{c,n}$ $(n = 1, 2, \ldots)$ . For a given $\mu$, the number of the intersections of the amplitude curves with a vertical line gives the number of solutions, which for $\Delta u = 1$ consists of PR and PZRh patterns. The figure also implies that $\mu_{c,n} - \mu_{c,n+1}$ is a monotonically decreasing function of $n$, and the $\lim_{n\to\infty} \mu_{c,n} = 0$, indicating that the number of oscillatory solutions diverges as the elastic anisotropy vanishes. Another

important feature of the figure is the amplitude ordering and amplitude growth with decreasing $\mu$. The amplitude of the shorter wave length mode is smaller than the bigger wave length mode. As typical of non-linear systems the amplitude growth is bounded.

Figure 2-9 shows the director orientation $\phi$ as a function of $u$, for $\mu = 0.01$, in which there are three solutions of PZRh (A,B,C) and one solution of PR (D). Figure 2-10 shows the eleven solutions for $\mu = 0.001$. As the figures show, by changing $\mu$ from 0.01 to 0.001, the number of the oscillatory solutions has increased from four to eleven. One can expect that as $\mu$ approaches zero, the number of branches will increase to infinity, meaning there will be infinite solutions to the equation. However, at any given finite value of $\mu$, there are only finite number of solutions to the system. Note that Fig. 2-9 and Fig. 2-10 show that the solution with higher frequency has

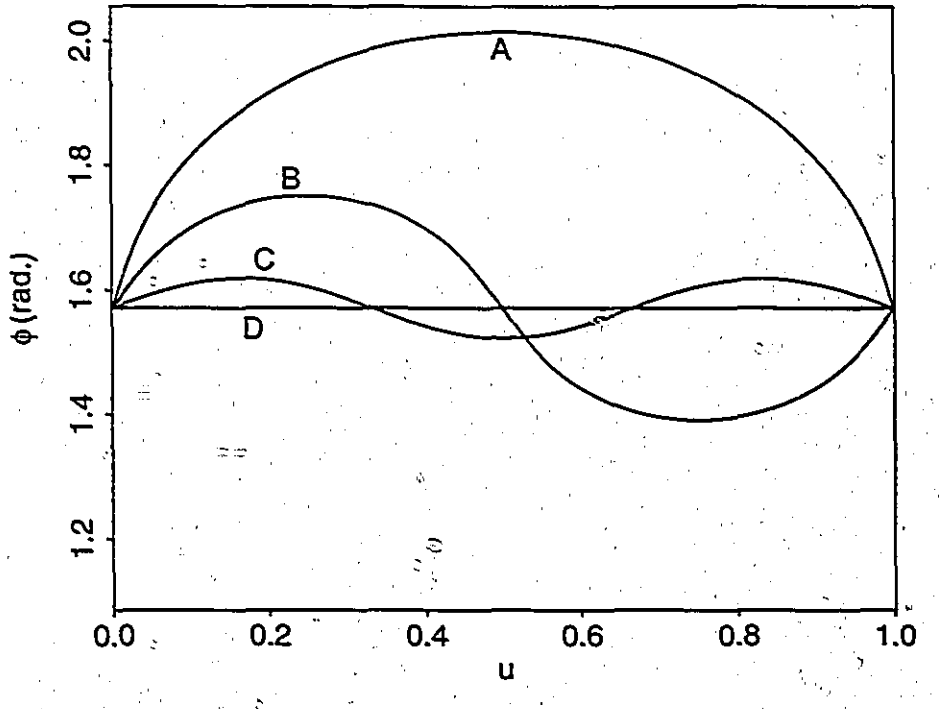


Figure 2-9: Director orientation $\phi(rad.)$ as a function of dimentionless distance $u$, for $\Delta u = 1$, $\mu = 0.01$ and $\phi(1) = \frac{\pi}{2}$. Curve D denotes the PR solutions while curves A, B, and C are members of PZRh family. The four solutions correspond to the four intersections of the horizontal line C with the curve in Fig. 2-11, for $\phi'(0) \geq 0$. The three mirror image oscillatory solutions are not shown.

smaller amplitude than those with lower frequency, which is a very important feature of

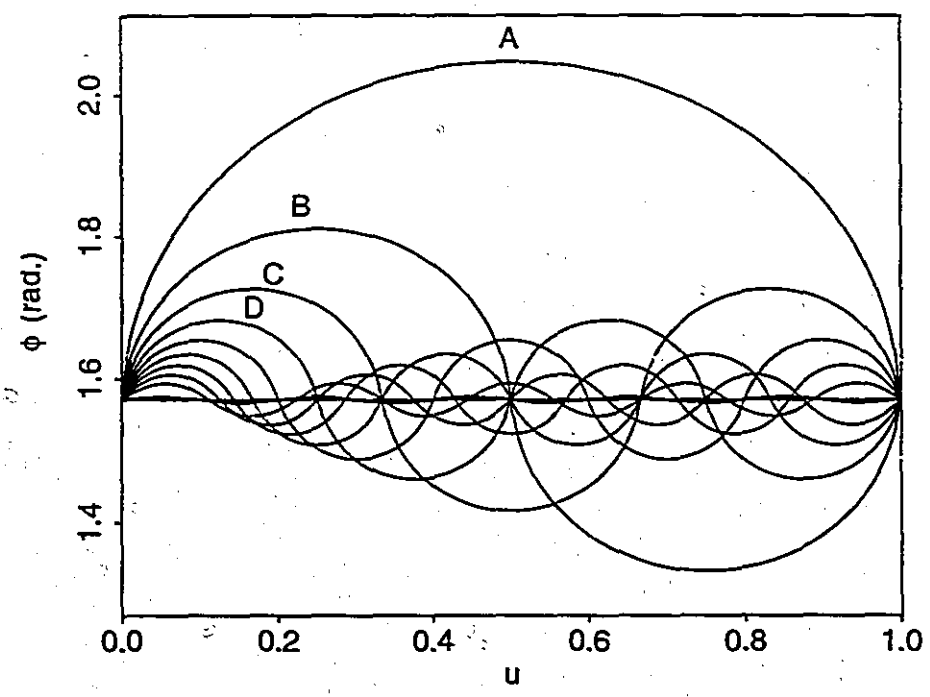


Figure 2-10: Director orientation $\phi(rad.)$ as a function of dimentionless distance $u$, for $\Delta u = 1$, $\mu = 0.001$ and $\phi(1) = \frac{\pi}{2}$. For this relatively small value of $\mu$ there are ten oscillatory solutions (PZRh) and the radial (PR) solution. Again, the mirror image oscillatory solutions are not shown for clarity. Note the significant increase in the number of solutions as $\mu$ changes from 0.01(Fig. 2-9) to 0.001.

the system.

As described in the previous section, the solutions are found by solving the extended system of equations (2.12) and initial conditions (2.13). In order to find all the solutions to the system, we plot in Fig. 2-11 the functional dependence of $\phi(1) - \phi(0)$ on $\phi'(0)$, for $\mu = 0.01$. The various horizontal lines correspond to various values of $\phi(1) - \phi(0)$. The line C represents the symmetric boundary conditions studied in this section (line A and B are discussed below), for which $\phi(1) = \phi(0) = \frac{\pi}{2}$. To find the number of solutions one can simply count the intersections of the horizontal lines with the curve. For line C, there are seven solutions: one trivial solution (PR), three oscillatory solutions (PRZh) with positive initial slop, and their three mirror images. (For brevity, we only show the oscillatory solutions with $\phi'(0) > 0$ in Fig. 2-9). It is clear from Fig. 2-11 that the above solutions are all the solutions of equation (2.9) for $\mu = 0.01$ and symmetric boundary

conditions.

To compare simulations with actual fiber textures (see for example Fig. 2-1 and [3, 4, 6]), it is useful to plot the molecular trajectories, i.e., the curves that are orthogonal to the local discotic director field. Similar to the streamline in fluid dynamics, the trajectory satisfies the geometrical relation: $tan(\psi)\frac{dr}{d\theta} = r$, where $\psi = \phi - \frac{\pi}{2}$. To find the trajectory $\theta(r)$ we integrate the above differential equation using the previously computed director field $\phi(r)$. Here $\theta$ is the usual polar angle in cylindrical coordinates. Figure 2-12 shows the scientific visualizations of the curves A, B, C and D in Fig. 2-10. The presence of spatial oscillations are clearly seen. In visualization A it is seen that the disk start with zero angle, indicating that the director angle is $\frac{\pi}{2}$. The trajectory shows an increase and then decrease of the director angle, ending at the outer boundary with the same angle as $\phi(0)$. In visualization B, corresponding to the solution with one full wave-length in Fig. 2-10, the oscillation is more visible. In visualizations C and D, there are more oscillations but with smaller amplitude.

Next we discuss the solution branching and texture behaviour of the PZRh pattern, for $\Delta u = 2$. Since $u(r_c) = 1$, this increment of $\Delta u$ corresponds to a larger outer radius. Figure 2-13 shows the director orientation as a function of $u$, for $\mu = 0.005$, corresponding to four members of the PZRh family. The figure shows that the main features of the oscillatory solutions remain invariant. For this parametric value we show four periodic solutions, again with higher amplitude corresponding to longer wave-length. Comparing the solution A in Fig. 2-13 to solution C in Fig. 2-10, it is seen that increasing $\Delta u$ results in amplitude growth. Again, to compare the theoretical results to actually patterns, we use visualizations, computed as described above. We note that in the visualization we have, without loss of information, kept the outer radius fixed. Figure 2-14 shows four visualizations (A,B,C,D) of members of the PZRh family, corresponding to the director profiles shown in Fig. 2-13. The multiple solutions suggest multiple configurations for the same set of elastic constants $K_1$ and $K_3$, which in reality would mean abundant oscillatory patterns. In these disk trajectories, we can see the finite amplitude oscillation that certainly captures the basic features of the cross-section of a mesophase carbon fiber displaying a radial zig-zag texture (see Fig. 2-1 and Fig.7 of [6]).

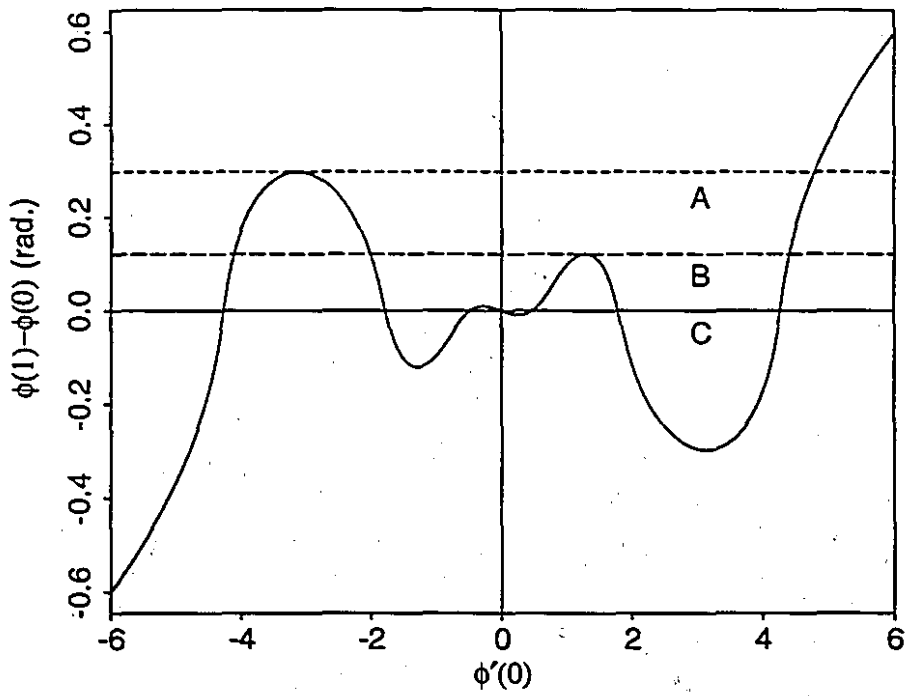


Figure 2-11: Functional relation of the outer boundary orientation $\phi(u_o)$ and the initial slop $\phi'(0)$, for $\Delta u = 1$ and $\mu = 0.01$. $\phi(1) - \phi(0)$: 0(full line C); 0.120(long dashed line B); 0.298(short dashed line A). Solutions to any value of outer boundary orientation can be found by drawing a horizontal line at the given value of $\phi(u_o)$, the initial slop of the solutions are given by the intersection of the line and the curve.

To establish the actual observability of the predicted spatially oscillatory radial zig-zag patterns, we have to determine the stability properties of the numerical solutions to equation (2.9). The most efficient way to examine the stability of the solutions obtained is to compute the second variation of the free energy integral [20]. By setting $\phi(u) = \phi^*(u) + \delta\phi(u)$ and expanding the free energy $F$ in power series of $\delta\phi(u)$ up to the second order, we get

$$\Delta F = \int [f(\phi^* + \delta\phi, \phi^{*\prime} + \delta\phi') - f(\phi^*, \phi^{*\prime})] du = (\delta F)_1 + (\delta F)_2 + \cdots \tag{2.14}$$

where

$$(\delta F)_1 = \int [\frac{\partial f}{\partial \phi} - \frac{d}{du}\frac{\partial f}{\partial \phi'}]_{\phi=\phi^*} du, \tag{2.15}$$

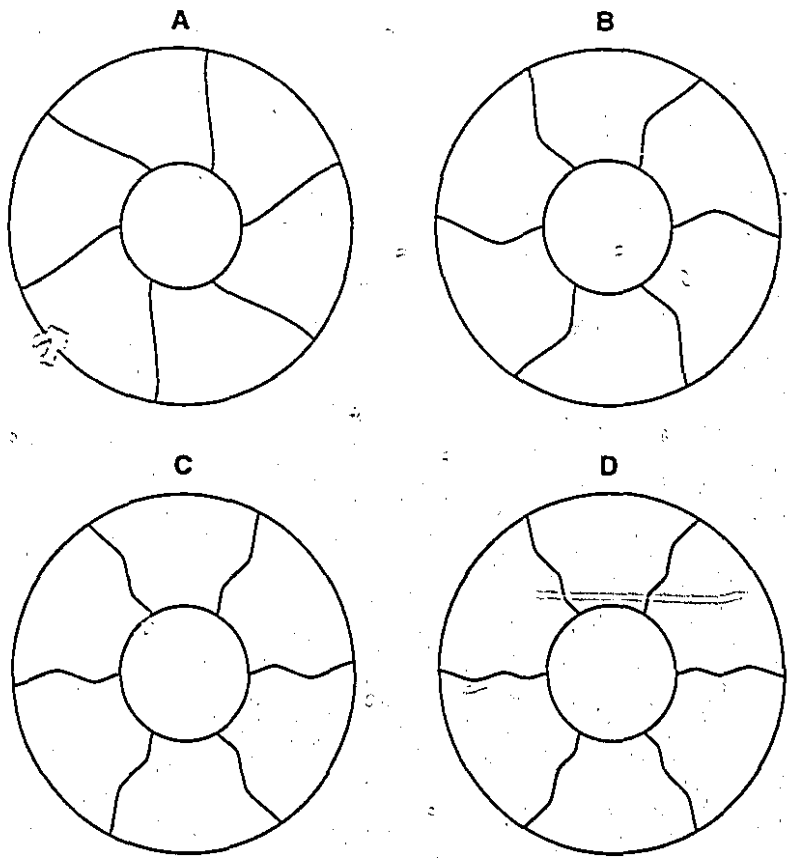


Figure 2-12: Director orientation $\phi(rad.)$ as a function of dimentionless distance $u$, for $\Delta u = 1$, $\mu = 0.01$ and $\phi(1) = \frac{\pi}{2}$. Curve D denotes the PR solutions while curves A, B, and C are members of PZRh family. The four solutions correspond to the four intersections of the horizontal line C with the curve in Fig. 2-11, for $\phi'(0) \geq 0$. The three mirror image oscillatory solutions are not shown.

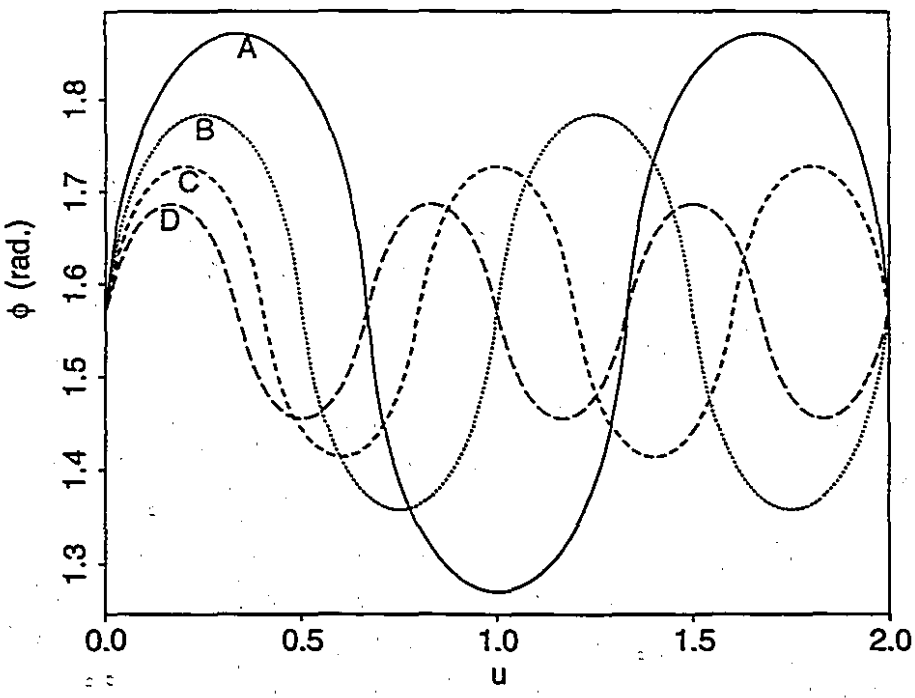


Figure 2-13: Director orientation $\phi(rad.)$ as a function of dimentionless distance $u$, for $\Delta u = 1$, $\mu = 0.001$ and $\phi(1) = \frac{\pi}{2}$. For this relatively small value of $\mu$ there are ten oscillatory solutions (PZRh) and the radial (PR) solution. Again, the mirror image oscillatory solutions are not shown for clarity. Note the significant increase in the number of solutions as $\mu$ changes from 0.01(Fig. 2-9) to 0.001.

and

$$(\delta F)_2 = \int [\frac{\partial^2 f}{\partial \phi^2}(\delta\phi)^2 + 2\frac{\partial^2 f}{\partial \phi \partial \phi'}\delta\phi\delta\phi' + \frac{\partial^2 f}{\partial \phi'^2}(\delta\phi')^2]_{\phi=\phi^*} du. \tag{2.16}$$

where $(\delta F)_1$ is the first variation of the free energy, and $(\delta F)_2$ is the second variation. By letting $(\delta F)_1 = 0$, we find the extremum free energy configuration $\phi^*$. Therefore, the sign of the increment $\Delta F$ coincides with the sign of $(\delta F)_2$. Replacing $f$ from equation (2.8), we obtain the following integral:

$$\begin{aligned}(\delta F)_2 = \int \{ & [K_3 - K_1](\cos 2\phi - 2\phi' \sin 2\phi - \phi'^2 \cos 2\phi)(\delta\phi)^2 \\ & + [K_3 - K_1](2\cos 2\phi - 2\phi' \sin 2\phi)\delta\phi\delta\phi' \\ & + (K_1 \sin^2\phi + K_3 \cos^2\phi)(\delta\phi')^2\} du\end{aligned} \tag{2.17}$$

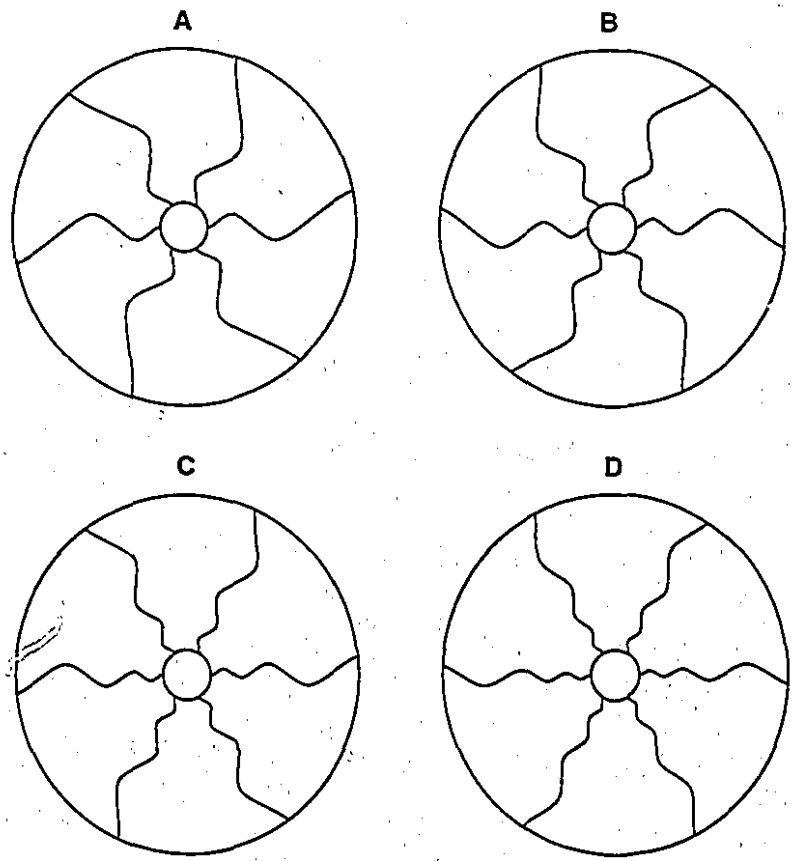


Figure 2-14: Scientific visualizations of disk trajectories for the oscillatory zig-zag (PZRh) solutions A, B, C, and D, shown in Fig. 2-10. The trajectories represent lines (of constant orientation) parallel to the molecular disks. Multiple oscillations are visible in B, C, and D.

Evaluating the integral for each of the numerical solutions, we compute the second variation of the free energy and thus are able to determine the free energy increment induced by an arbitrary small perturbation. Fig. 2-15 shows the second variation $(\delta F)_2$ as a function of the amplitude of an oscillatory solution belonging to the PZRh patterns. The parametric conditions are $\mu = 0.001$ and $\Delta u = 1$. The dots in Fig. 2-15 are second variations of the oscillatory solutions whose director profiles are shown in Fig. 2-10. The figure shows that the second variation is always positive. Therefore, based on the argument above, all the oscillatory solutions are locally stable to small perturbations. We may conclude that the oscillatory trajectories are the stable configurations for this type of boundary condition, thus proving abundant multistability. As in other non-linear systems that exhibit multistability, a specific member of the PZRh family will be selected if the initial conditions are included in the domain of attraction of that particular solution. Since the domain of attractions of the various solutions are function of $(\mu, \Delta u, \phi(u_o) - \phi(0))$, a particular initial texture may evolve to different members of the PZR family, according to the governing parameter values.

The second variation method is successful in estabilishing the stability of the oscillatory solutions, however, it fails for the trivial solution. In the integral (2.16), one can see that substituting the trivial solution gives $\phi^* = constant$, $\delta\phi = 0$, and $\delta\phi' = 0$, and thus the integral will be zero. In fact, for the trivial solution any variation will be identically zero. Therefore we can not determine the stability of trivial solution under any given parametric conditions using this method and have to use another analytical method. Consider a small perturbation on the constant solution [10],

$$\phi(u) = \frac{\pi}{2} + \delta(u), \tag{2.18}$$

where $\delta(u)$ is a small perturbation which satisfies

$$\delta(0) = \delta(1) = 0. \tag{2.19}$$

Substitute (2.18) into equation (2.8) and expand the result, then the energy density

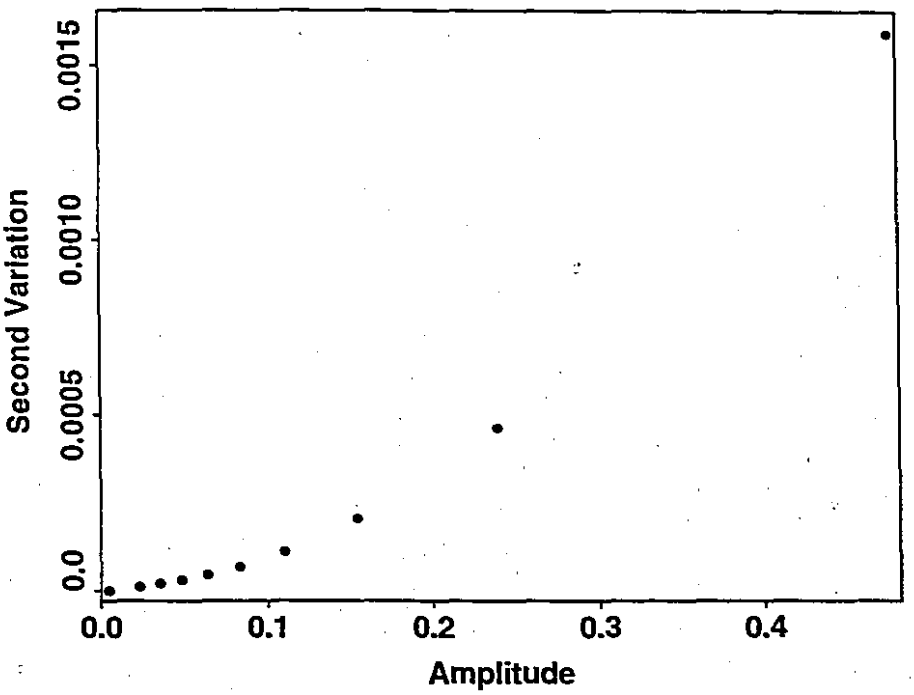


Figure 2-15: Second variation $\delta F_2$ of the free energy as a function of the amplitude for the oscillatory zig-zag (PZRh) solutions shown in Fig. 2-10. Since $\delta F_2 > 0$ the oscillatory zig-zag solutions are all locally stable, thus proving the presence of multistability phenomena.

difference to second order is given by:

$$f_2 = \frac{K_1}{2}(\delta^2 + 2\delta'\delta + \delta'^2) + \frac{K_3}{2}(-\delta^2 - 2\delta\delta') \tag{2.20}$$

Applying the above expression in the free energy integral, using integration by parts, and taking into account the boundary condition of $\delta(u)$, the difference of the total free energy will be

$$\begin{aligned} \Delta F &= \int f_2 du \\ &= \frac{1}{2}\int \{K_1(\delta^2 + 2\delta\delta' + \delta'^2) + K_3(-\delta^2 - 2\delta\delta')\} du \\ &= \frac{1}{2}\int \{(K_1 - K_3)\delta - K_1\delta''\}\delta du \end{aligned} \tag{2.21}$$

If the above integral is positive, then the configuration is stable to small perturbations. If

the integral is positive, it means any small perturbation will increase the total free energy, thus the constant solution would be a local minimum of the free energy and therefore is stable to any perturbation. To determine if the integral is positive, we therefore consider the following eigenvalue problem:

$$\frac{K_1 - K_3}{2}\delta - \frac{K_1}{2}\delta'' = \lambda\delta, \tag{2.22}$$

with the boundary conditions of $\delta(0) = \delta(1) = 0$. When the above eigenvalue problem has positive eigenvalues, that is $\lambda > 0$, then the free energy integral becomes

$$\Delta F = \frac{1}{2}\int\{(K_1 - K_3)\delta - K_1\delta''\}\delta du = \int \lambda\delta^2 du \tag{2.23}$$

which is positive definite, and we can then determine the stability of the configuration based on the previous argument. Solving the eigenvalue equation, we obtain:

$$\lambda = \frac{1}{2}\{K_1 - K_3 + K_1(\frac{n\pi}{\Delta u})^2\}; (n = 1, 2, 3, \ldots) \tag{2.24}$$

It follows that if $\lambda < 0$, the pure bend (radial) structure will be unstable to any small perturbation. We find the stability threshold of the radial texture is:

$$\mu < \mu_{c,n} = \frac{1}{1 + (\frac{n\pi}{\Delta u})^2}; (n = 1, 2, 3, \ldots) \tag{2.25}$$

Putting $\Delta u = 1$ and $n = 1$ in the above inequality, we find $\mu_{c,1} = 0.092$, which is equal to the value of $\mu$ corresponding to the bifurcation point found numerically, reported above in this section. A comparison of analytical values and the numerical values of $\mu_{c,n}$ is shown in the Table I.

Table I: Elastic anisotropy ($\mu$) thresholds for birth of oscillatory modes

| $\mu_{c,n}$ | *theoretical value* | *numerical value* |
|---|---|---|
| $n=1$ | 0.09199 | 0.09200 |
| $n=2$ | 0.02470 | 0.02500 |
| $n=3$ | 0.01113 | 0.01127 |
| $n=4$ | 0.006293 | 0.006265 |
| $n=5$ | 0.004036 | 0.003999 |

The excellent agreement validates the correctness of the numerical results.

According to the general theory of eigenvalue problems, the eigenvalues obtained for equation (2.22) present the values of $\lambda_n$ at which nontrivial solutions can be found. The existence of nontrivial solutions for these values of $\lambda_n$, which corresponds to the values of $\mu_{c,n}$, arise from the bifurcations of the constant solution branch at these points. The exact correspondence between the eigenvalues and the bifurcations is the reason behind the consistency between analytical and numerical results, as shown in Table I. In addition, the small amplitude oscillatory solutions can be closely approximated by the corresponding eigenfunctions derived above. A discussion giving the mathematical details of the eigenvalue problem is given in the Appendix.

According to the inequality (2.25), the value of $\mu_{c,1}$ depends on $\Delta u$. For all $\Delta u$, $\mu_{c,1}$ is always a positive number and $\mu_{c,1} \leq k$, where $k < 1$. This means the bifurcation will not occur as soon as $K_1 < K_3$, instead, the trivial solution will still be stable until the ratio $\frac{K_1}{K_3}$ exceeds a certain critical threshold $\mu_{c,1}$. As $\Delta u$ increases, $\mu_{c,1}$ increases accordingly. So, for $\Delta u > 1$, the critical value of $\mu_{c,1}$ can be very close to 1. Therefore for relatively large fibers, a small elastic anisotropy of the type studied here ($\mu < 1$, that is, the bend constant larger than the splay constant) will induce a bifurcation in the equation (2.9), corresponding to a transformation between the radial texture and the zig-zag radial texture. This is a reason for the frequent observation of oscillatory zig-zag textures in actual mesophase fibers [6].

Although this chapter is restricted to patterns that arise from continuous transformations of the ideal pure bend planar radial pattern, here we briefly discuss a significant

fact regarding the stability of the onion patterns in the presence of $\mu < 1$ (see Fig. 2-1) since this has direct relevance to our objectives. In contrast to the frequently observed zig-zagging in radial patterns, oscillations and zig-zagging of the onion patterns have apparently not been reported. It is thus important to explain this absence, and at the same time establish that our criteria that lead to the frequently observed PZRh patterns would not lead to zig-zagging in the onion texture, thus adding validity to our analysis. The onion pattern is found for symmetric boundary conditions: $\phi(0) = \phi(1) = 0$. The trivial solution for this type of boundary condition is $\phi = 0$. This type of configuration represents a pure splay mode, that is, the concentric texture. To determine its stability, we follow the same method elaborated above, and add a small perturbation $\delta(u)$ to the trivial solution,

$$\phi = \delta(u) \tag{2.26}$$

with boundary condition of $\delta(0) = \delta(1) = 0$. Then to second order, the perturbed energy is given by:

$$f_2 = \frac{K_1}{2}(-\delta^2 - 2\delta'\delta) + \frac{K_3}{2}(\delta^2 + 2\delta'\delta + \delta'^2) \tag{2.27}$$

Thus we obtain:

$$\Delta F = \int f_2 du = \frac{1}{2}\int \{(K_3 - K_1)\delta - K_3\delta''\}\delta du \tag{2.28}$$

Similarly, we consider the eigenvalue problem of

$$\frac{K_3 - K_1}{2}\delta - \frac{K_3}{2}\delta'' = \lambda\delta, \tag{2.29}$$

with boundary condition of $\delta(0) = \delta(1) = 0$. The eigenvalues now are given by:

$$\lambda = \frac{1}{2}\{K_3 - K_1 + K_3(\frac{n\pi}{\Delta u})^2\}, (n = 1, 2, 3, \ldots) \tag{2.30}$$

It follows that, if $K_1 < K_3$, when the radial oscillatory patterns are often observed, the eigenvalues in (2.30) will always be positive, and the onion pattern will be stable to any small perturbations. Therefore, there is no oscillatory solution to the equilibrium equation under this type of boundary and elastic anisotropy conditions. Hence there will

be no oscillations to the pure splay mode, any perturbations to this pattern will decay to zero, and a zig-zag onion pattern would never occur, which is in agreement with the facts.

### 2.5.2 Solutions with asymmetric boundary conditions

In this section we analyze the new features arising from non-symmetric boundary conditions: $\phi(0) = \frac{\pi}{2}, \phi(1) = \alpha$, with $\frac{\pi}{2} < \alpha < \pi$. The first important feature is that the PR pattern does not exist, and its role is taken up by the planar pinwheel pattern PPW. Instabilities deduced by elastic anisotropies lead to bifurcations involving PPW and PZRn branches, here PZRn stands for planar non-homeotropic zig-zag radial pattern (see Fig. 2-4).

As shown in the second row of Fig. 2-6, for $\phi(1) = 1.869$, the solution for $\mu > 1$ is unique and monotonic. For $\mu = 1$, the solution is linear. We can derive this linear solution analytically. By setting $K_1 = K_3$ in the equilibrium equation, we find

$$K_1 \phi'' = 0 \tag{2.31}$$

and the equation has a unique linear solution for $K_1 = K_3$.

For $\mu < 1$, similar to the situation with symmetric boundary conditions, the bifurcation will not occur until $\mu$ exceeds the critical value of $\mu_{c,1}$, but now $\mu_{c,1}$ will be a function of $\phi(u_o)$ as well as of $\Delta u$. Figure 2-16 shows the computed bifurcation diagram in the $(\mu, \phi(u_o))$ plane. The full line denotes the bifurcation for $\Delta u = 1$; for symmetric boundary condition, i.e. $\phi(1) = \phi(0) = \frac{\pi}{2}$, the bifurcation occurs at $\mu_{c,1} = 0.092$. As $\phi(1)$ increases, the critical value of bifurcation $\mu_{c,1}$ decreases. Above the full line, equation (2.9) has a unique locally stable monotonic solution (PPW), and below the full line the equation has multiple locally stable solutions (PZRn). The dashed line denotes the bifurcation between PPW and PZRn, for $\Delta u = 2$. Note the significant increase of $\mu_c$ as $\Delta u$ increases. For $\Delta u = 2$ with symmetric boundary conditions, the bifurcation occurs at $\mu = 0.285$. When substituting $\Delta u = 2$ into the inequality (2.25), we obtain $\mu_c = 0.288$, which agrees with the numerical results. Again above the dashed line the locally stable

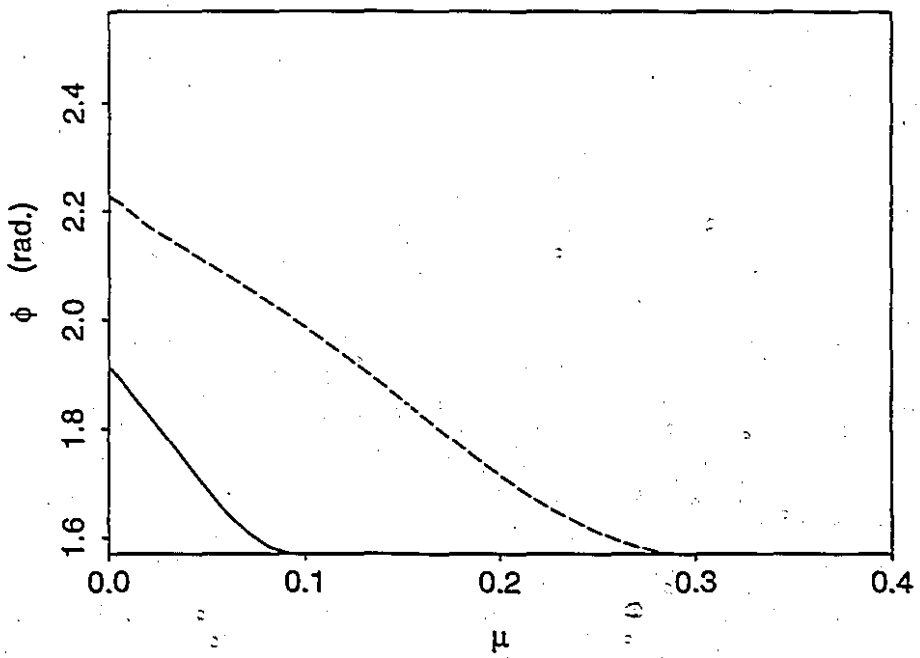


Figure 2-16: Bifurcation diagram in the elastic anisotropy $\mu$ outer boundary condition plane. Fiber size $\Delta u = 1$ (full line), 2 (dashed line). The full (dashed) line divides the parametric plane into two solution regions. The one above the line is where equation (2.9) has a unique solution, and the one below the line as well as the line itself is where the equation has multiple oscillatory solutions.

solutions are PPW solutions, while below the dashed line there are multiple locally stable PZRn solutions.

For $\mu_{c,1} < \mu < 1$, the equation has a unique nonlinear monotonic solution, representing the PPW pattern. The difference between solutions for $\mu < 1$ and solutions for $\mu > 1$ is their concavity, as shown in the panels of the middle row of Fig. 2-6. The change of concavity is due to the change of elastic constants which make splay deformation more favorable for $K_1 < K_3$, and bend deformation favorable for $K_1 > K_3$. Below the dashed line, when $\mu < \mu_{c,1}$, the system will have multiple solutions. The functional relation of $\phi'(0)$ and $\phi(1)$ shown in Figure 2-11 can also be used to find the solutions for asymmetric boundary conditions; line A corresponds to $\phi(1) = 1.868761$, and line B to $\phi(1) = 1.692094$. As shown in Figure 2-11, there are two solutions for $\phi(1) = 1.868761$, and four solutions for $\phi(1) = 1.692094$. Figure 2-17 shows the director orientation $\phi$ as

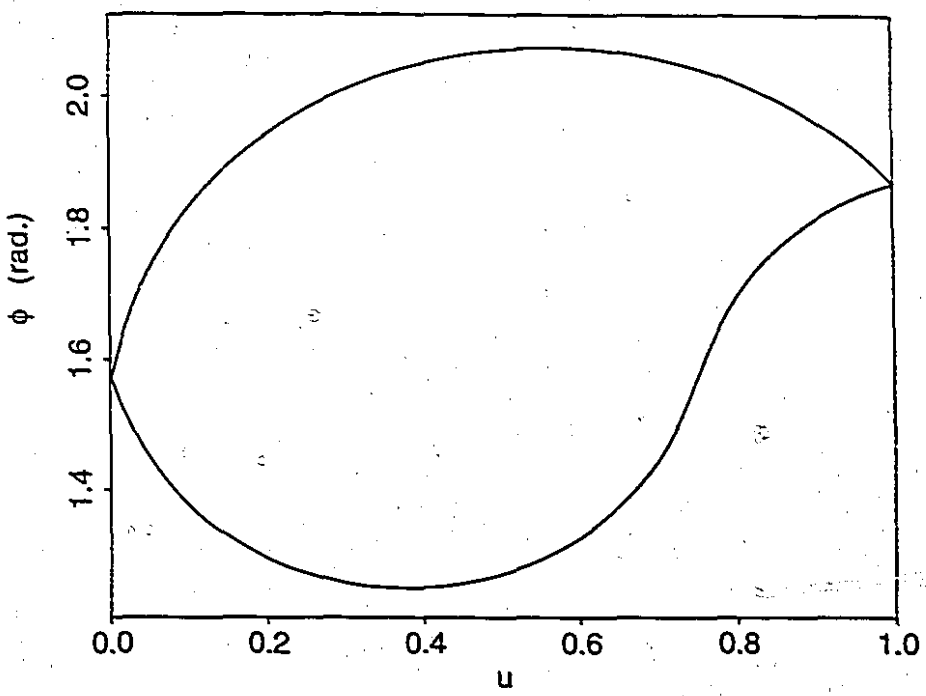


Figure 2-17: Director orientation $\phi(rad.)$ as a function of $u$, for $\Delta u = 1$, $\mu = 0.01$ and $\phi(1) = 1.868$. The two solutions are members of the PZRn family. They correspond to the two intersections of line A with the curve in Fig. 2-11.

a function of $u$, for $\phi(1) = 1.868761$ and $\mu = 0.01$, corresponding to the solutions found from line A in Fig. 2-11. The two solutions are members of the PZRn family, with the upper curve representing the first mode and the lower curve the second mode. Figure 2-18 shows the director orientation $\phi$ as a function of $u$, for $\phi(1) = 1.692094$ and $\mu = 0.01$, corresponding to the solutions found from line B in Fig. 2-11. The four solutions are members of the PZRn family. Following the visualization methodology presented above, Fig. 2-19 shows the disk trajectories for the four solutions (A,B,C,D) shown in Fig. 2-18. Since solutions A and D in Fig. 2-18 display incomplete oscillations, the corresponding disk trajectories also display incomplete oscillation. For solution B and C in Fig. 2-18, the oscillations in the disk trajectories are clearer.

Again here we wish to explore the role of fiber size on the main features of the bifurcation and multistability by plotting the trajectories of PPW and PZRn patterns. Figure 2-20 shows four solutions for $\Delta u = 2$, $\mu = 0.005$, and $\phi(2) = 1.3(rad.)$ , which

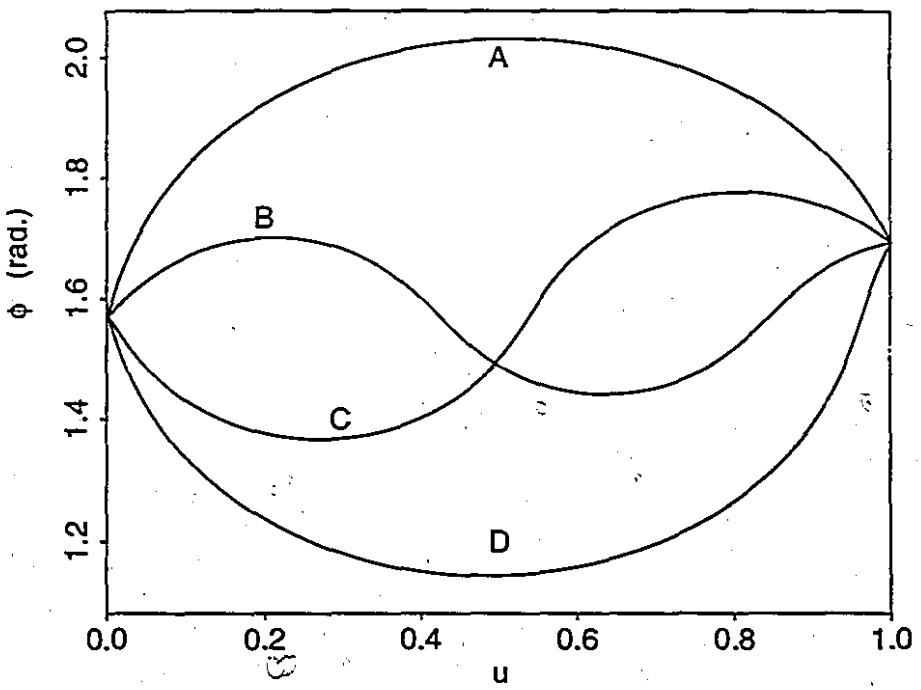


Figure 2-18: Director orientation $\phi(rad.)$ as a function of $u$, for $\Delta u = 1$, $\mu = 0.01$ and $\phi(1) = 1.692$. The four solutions are members of the PZRn family. They correspond to the four intersections of line B with the curve in Fig. 2-11.

belong to the PZRn family. The corresponding visualization of disk trajectories are shown in Fig. 2-21. Here, as in the previous section, an increase in $\Delta u$ brings an increase in the amplitude in the oscillations. For the disk trajectories representing solution B and C in Fig. 2-20, one can clearly see the oscillations to avoid free energy costs.

In the following we explore the main difference that arise in the solution behaviour and multistability phenomena, in the presence of symmetric and asymmetric boundary conditions. Figure 2-11 shows that the solutions are not symmetric as in the case of symmetric boundary conditions. For solutions with $\phi(1) = 1.692094$, the mirror configurations are the solutions at $\phi(1)_{mirror} = \pi - \phi(1)$. Another feature that is different from the case with symmetric boundary condition, is that as $\mu$ decrease further, the number of solutions will increase to a certain finite value, which depends on the value of boundary orientation at the outer cylinder, as opposed to the monotonic increase in the number of solutions (PZRh) for symmetric boundary conditions. The reason is that

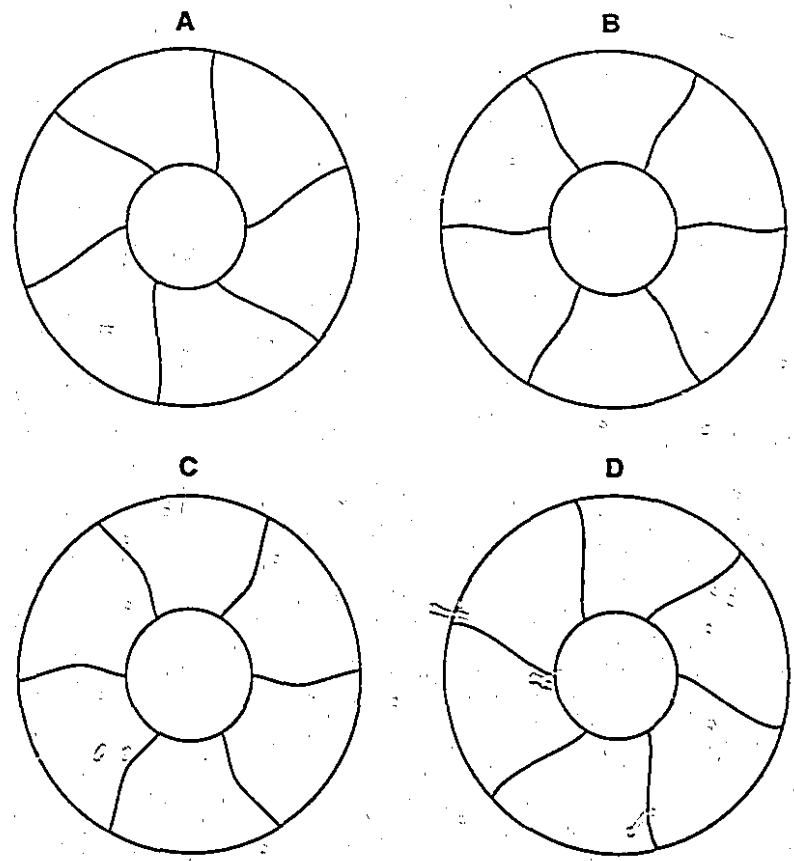


Figure 2-19: Scientific visualizations of disk trajectories for the oscillatory zig-zag (PZRn) solutions A, B, C, and D, shown in Fig 2-18. Finite amplitude oscillations are visible in B and C. The different spiral directions in A and D are due to the different values of $\phi'(0)$ for solution A and D in Fig. 2-18.

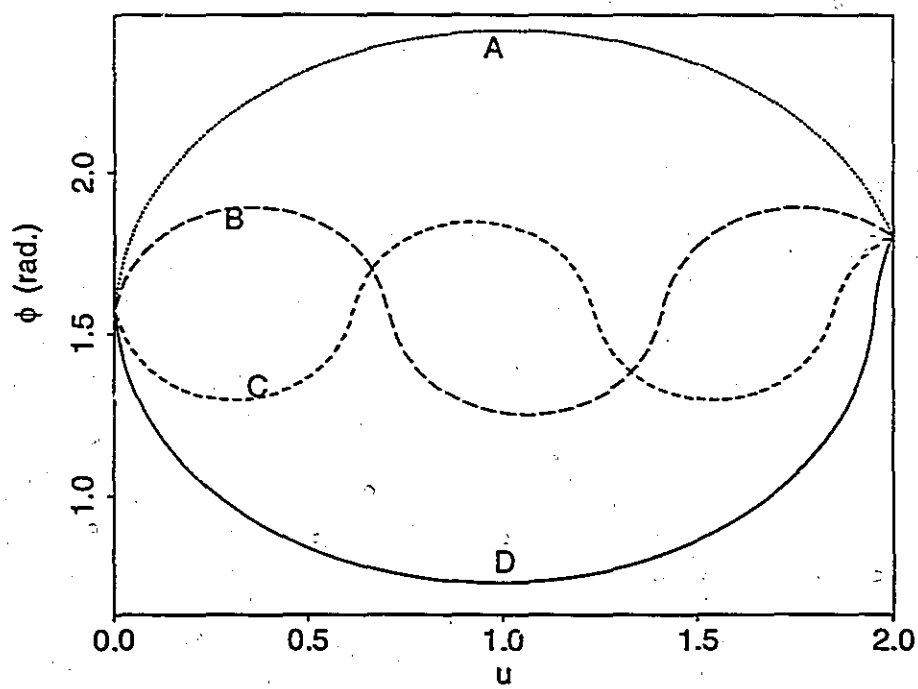


Figure 2-20: Director orientation $\phi(rad.)$ as a function of $u$, for $\Delta u = 2$, $\mu = 0.005$ and $\phi(2) = \frac{\pi}{2}$. The solutions are members of the PZRn family. Note the amplitude increase for these solutions in comparison to the PZRn solutions with the same wave numbers but smaller $\Delta u (\Delta u = 1)$ shown in Fig. 2-18.

for oscillatory PZRn and PZRh solutions, the solution amplitude has to be larger than $\phi(u_o) - \phi(0)$. However, since a solution with higher frequency has smaller amplitude, and the lowest possible amplitude would be $\phi(u_o) - \phi(0)$, therefore even if $\mu$ continues to decrease, there will be no new solutions and the number of solutions with amplitude larger than $\phi(u_o) - \phi(0)$ will therefore always be finite.

### 2.5.3 Solutions for asymmetric boundary conditions with large asymmetry

In this section we briefly explore the new phenomena that arise due to large asymmetry in the boundary conditions, and report on the representative case of $\phi(u_o) = \pi$. For the case with boundary condition of $\phi(0) = \frac{\pi}{2}, \phi(1) = \pi$, we find only one solution for all different value of $\mu$, as shown in the third row of Fig. 2-6. Again, the concavity of the

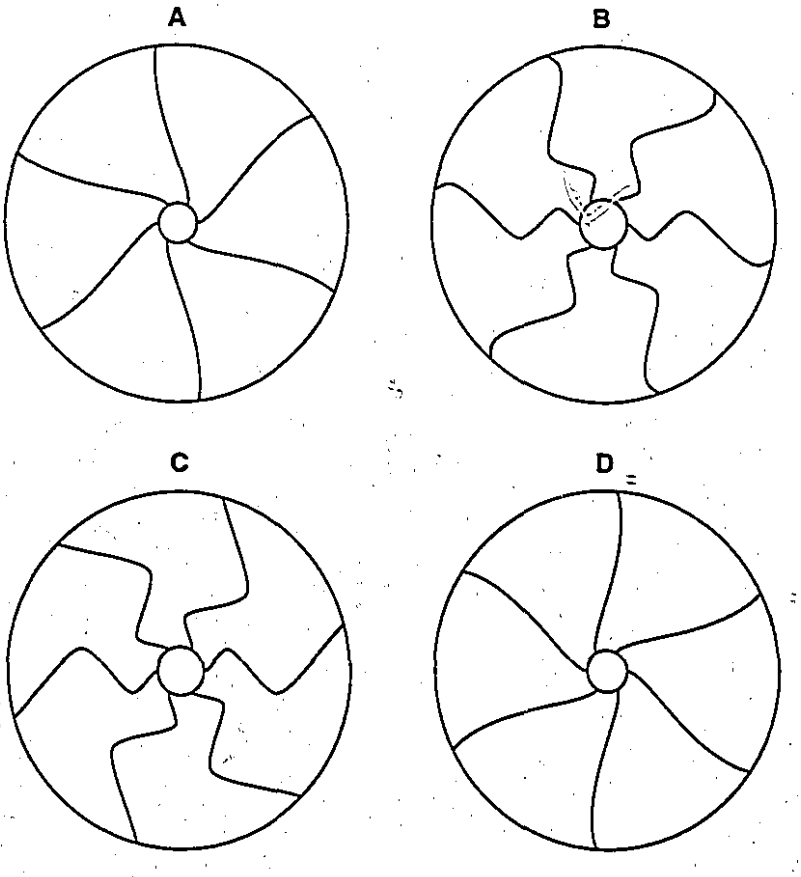


Figure 2-21: Scientific visualizations of disk trajectories for the oscillatory zig-zag (PZRn) solutions A, B, C, and D, shown in Fig. 2-20.

solution will change as $\mu$ changes from $\mu > 1$ to $\mu < 1$. As $\mu$ diverges ($\mu \to \infty$) the solution is boundary-layer like, with the boundary layer located next to $u = 1$. While when $\mu$ vanishes ($\mu \to 0$) the boundary layer is located next to $u = 0$. Figure 2-22 shows the director orientation $\phi$ as a function of $u$, for three different values of $\mu$: 1000 (dashed), 1 (dotted), and 0.001 (full). The linear solution is obtained for $K_1 = K_3$ ($\mu = 1$), and the concavity of the other two curves is in agreement with the expected boundary layer mode that minimizes the free energy.

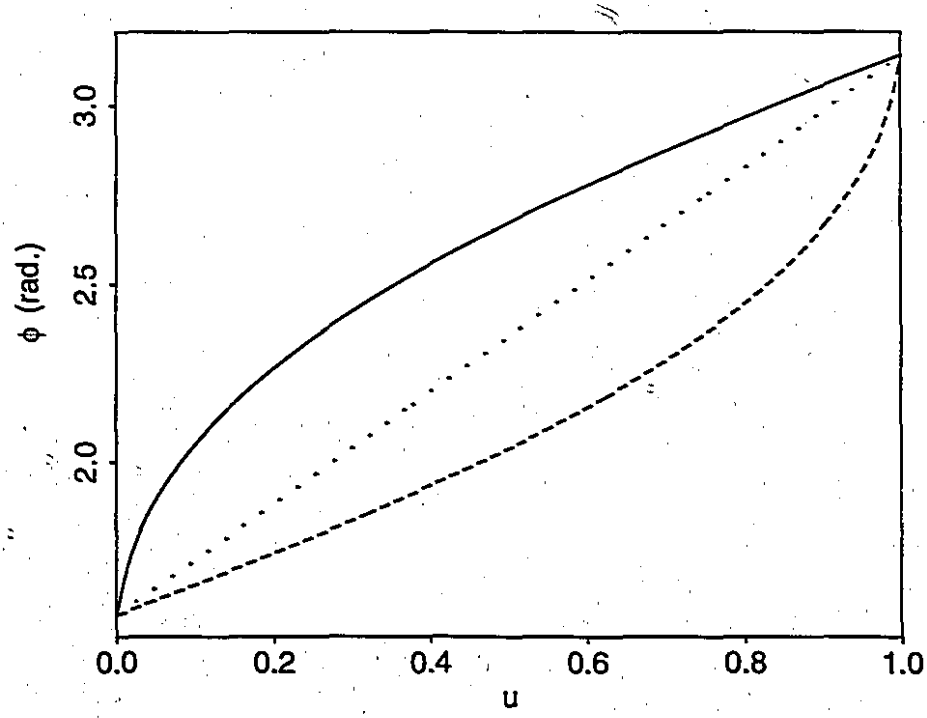


Figure 2-22: Director orientation $\phi(rad.)$ as a function of $u$, for $\Delta u = 1$ and $\phi(1) = \pi$, for $\mu$: 0.001 (full line); 1 (dotted line); 1000 (dashed line). For $\mu_1 = 1$ ($K_1 = K_3$) the solution is linear, for $\mu_1 \ll 1$ ($K_1 \ll K_3$) the solution is concave down, and for $\mu_1 \gg 1$ ($K_1 \gg K_3$) concave up, as dictated by energy minimization.

For this type of boundary condition, there are no bifurcation in the equilibrium equation (2.9). As shown above, the amplitude of any oscillatory solution has to be larger or equal to $\phi(u_o) - \phi(u_c)$, which in the present case is $\frac{\pi}{2}$. However, since the increase of frequency of any solution will result in a decrease in amplitude and the existing monotonic solution has an amplitude of $\frac{\pi}{2}$, any oscillatory solution would have to have an amplitude

less than $\frac{\pi}{2}$, yet it has to have a maximum of $\phi(u_o) = \pi$ in order to satisfy the boundary condition at the outer cylinder. The contradiction makes the existence of oscillatory solutions impossible. Therefore we can conclude that for this type of boundary conditions, there exists no oscillatory solutions to equation (2.9) at any value of $\mu$.

In this section we have presented numerical results for three types of boundary conditions. A summary of the results is shown in Table II. In general, for symmetric type of boundary conditions of $\phi(u_c) = \phi(u_o) = \frac{\pi}{2}$, equation (2.9) has a unique constant solution for $\mu > \mu_{c,1}$. When $\mu < \mu_{c,1}$, the constant solution becomes unstable to small perturbations, the system undergoes a bifurcation and generates a family of branches of oscillatory solutions (PRZh). For symmetric boundary condition of $\phi(u_c) = \phi(u_o) = 0$, we have shown that while $\mu < 1$ there is only constant solution to the equation. For asymmetric boundary conditions with $\phi(u_c) = \frac{\pi}{2}$ and $\phi(u_o) < \pi$, the equation has a unique monotonic solution (PPW) for $\mu > \mu_c$. Particularly, at $K_1 = K_3$, the equation has a unique linear solution. As $\mu < \tilde{\mu}_c$, the system will bifurcate and generate branches of oscillatory solutions (PZRn). For asymmetric boundary condition of $\phi(u_o) = \pi$, there is a unique monotonic solution (PPW) to the equation for all value of $\mu$.

Table II: Summary of parametric ranges and stability properties of orientation textures

| *Boundary condition* $\phi(0) = \frac{\pi}{2}$ | $\mu = \frac{K_1}{K_3}$ | *Solution type* | *Figures* |
|---|---|---|---|
| $\phi(u_o) = \frac{\pi}{2}$ | $\mu > 1$ | PR<br>stable | 2-6 |
| | $\mu = 1$ | PR<br>stable | 2-6 |
| | $\mu_c < \mu < 1$ | PR<br>stable | 2-6 |
| | $\mu < \mu_c$ | PZRh<br>stable | 2-9,2-10,2-13 |
| $\frac{\pi}{2} < \phi(u_o) < \pi$ | $\mu > 1$ | PPW<br>concaving up, stable | 2-6 |
| | $\mu = 1$ | PPW<br>stable | 2-6 |
| | $\mu_c < \mu < 1$ | PPW<br>concaving down, stable | 2-6 |
| | $\mu < \mu_c$ | PZRh<br>stable | 2-17,2-18,2-20 |
| $\phi(u_o) = \pi$ | $\mu > 1$ | PPW<br>concaving up, stable | 2-22 |
| | $\mu = 1$ | PPW<br>stable | 2-22 |
| | $\mu < 1$ | PPW<br>concaving down, stable | 2-22 |

**PR: planar radial pattern, PZRh: homeotropic planar zig-zag radial pattern, PZRn: non-homeotropic planar zig-zag radial pattern, PPW: planar pinwheel pattern.**

## 2.6 Conclusion

In summary, we have presented a detailed numerical analysis to a model that is sufficiently accurate to provide plausible explanation to the pattern formation process that arises during the industrial melt fiber spinning of carbonaceous mesophases, using discotic nematic liquid crystal precursors. In addition, a comprehensive analysis of pattern formation in discotic nematics confined to an annular geometry has been presented. Numerical studies of the solution types to the equilibrium equation (2.9) derived from Frank's elastic energy model indicate that the equilibrium equation displays a wide variety of solution types in the parametric space spanned by the elastic anisotropy, the fiber diameter, and the boundary conditions. The basic planar patterns with singular cores are the radial pattern, the pinwheel pattern, and the zig-zag radial pattern. Only the zig-zag radial pattern exhibit multistability. Multistability of oscillatory solutions displaying the radial zig-zag patterns are found for: larger elastic anisotropy ($K_3 > K_1$), weaker boundary condition asymmetries, and larger fibers.

Numerical as well as analytical results show that the occurrence of oscillations in radial patterns is due to the elastic splay-bend anisotropy. This is because the energy minimization process of the free energy would select the most cost-effective pattern to lower the total free energy. Therefore, as the bend configuration becomes costly, the system will naturally select splay deformation over the bend deformations. Another point to be noticed is the effect of fiber size on the radial patterns. It is shown that larger fibers have a much greater tendency than smaller fibers to generate oscillatory radial patterns under the same elastic anisotropy conditions. In this case, the pattern selected by the free energy minimization process, is resisted by the effect of boundary orientation constraints that is in favor of an energy costly mode. This is also the reason why oscillatory patterns will not arise as soon as the elastic constants become different. Instead, the driving force minimizing the free energy due to elastic anisotropy has to overcome the resistance due to the boundary orientation constraint. As the fiber size becomes larger, the effect of such boundary constraints is weakened. Therefore in larger fibers the boundary orientation will have smaller effect on pattern selection, and elastic

anisotropy will have a stronger influence. Thus, oscillatory radial patterns will be easier to be observed in larger fibers than in small fibers. As for the non-homeotropic case, in which the outer boundary orientation is different from the inner boundary orientation, because the pattern consists of a splay-bend mode, the selection of oscillatory patterns would have much less effect on minimizing the free energy than it has on pure bend mode, for the same elastic anisotropy. Therefore, for the same geometric conditions, non-homeotropic boundary orientations would require a stronger elastic anisotropy to induce oscillatory patterns, as shown in this chapter.

To determine the stability of any solution, we computed the corresponding second variation of the elastic energy. The oscillatory solutions (PZRi, i=n,h) to the equilibrium equation are shown to be locally stable, whereas the stability of the trivial solution would depend on the ratio of the elastic constants and the ratio of the radii of the outer cylinder and the inner cylinder, as shown by analytical methods.

The interpretation of the numerical results using classical liquid crystal physics leads to explanations of pattern formation phenomena that arise in an industrial process. The elastic anisotropy, which is characterized by the ratio of the two elastic constants $K_1$ and $K_3$, representing the splay and bend deformations, is shown to be the driving force behind the pattern selection mechanism, that leads to the formation of the planar zig-zag pattern, frequently observed during fiber spinning.

# Bibliography


[1] Singer L.S., Faraday Discuss. Chem. Soc. **79**,265(1985).

[2] Edie D.D., Dunham M.G., Carbon, **27**, 647(1989).

[3] Fathollahi B., White J.L., J. Rheol. **38**(5), 1591(1994).

[4] Honda H., Mol. Cryst. Liq Cryst. **94**,97(1983).

[5] de Gennes P.G. and Prost J., *The Physics of Liquid Crystals*, 2nd ed. (Clarendo, Oxford, 1993).

[6] Pencock G.M., Taylor G.H. and FitzGerald J.D., Carbon **31**, 591(1993).

[7] Krali S., Zumer S., Phys. Rev. E, 366-379(1995).

[8] Marroum R.M., Iannacchione G.S., Finotello D., Lee M.A., Phys. Rev. E, R2473(1995).

[9] Rey A.D., Phys. Rev. E, **51**, 6278(1995).

[10] Tsuru H., J. Phys. Soc. Jpn. **59**, 1600(1990).

[11] Williams D.R.M., Phys. Rev. E **50**, 1686(1994).

[12] Crowford G.P., Allender D.W., Doane J.W., Vilfan M., Vilfan I., Phys. Rev. A, **44**, 2570(1991).

[13] Sokalski K. and Ruijgrok Th.W., Physica A **113**, 126(1982).

[14] Baals H., Hess S. and Naturforsh Z.. Teil A **43**, 662(1988).

[15] Warmedan T., Frenkel D. and Zijlstra R.J.J., J. Phys. (Paris) 48, 319(1987).

[16] Lee S.D., and Meyer R.B., in *Liquid Crystallinity in Polymers*, edited by A. Ciferri (VCH, New York, 1991), p. 343.

[17] Bird R.B., Curtis C.F., Armstrong R.G. and Hassager O., *Dynamics of Polymer Liquids* (Wiley, New York, 1987), Vol. 1.

[18] Singh A.P. and Rey A.D., J. Phys. II (Paris) 4, 645(1994)

[19] Ascher U.M., Mattheij R.M. and Russell R.D., *Numerical Solution of Boundary Value Problems for Odinary Differetial Equations*, (Prentice Hall, New Jersey, 1988).

[20] Barbero G., Mol. Cryst. Liq. Cryst. **195**, 199(1991).

[21] Troger H. and Steindl A., *Nonlinear Stability and Bifurcation Theory*, (Springer-Verlag, New York, 1991).

# Chapter 3

# Pattern selection mechanism in mesophase carbon fibers

## 3.1 Summary

Carbonaceous mesophases are spun into high performance carbon fibers using the melt spinning process. The spinning process produces a wide range of different fiber textures whose origins are not well understood. The cross-section fiber texture is a strong function of temperature, such that at lower temperatures the selected pattern is known as radial, while at higher temperatures it is known as onion. More intriguing and unexpected is the random pattern that is found at intermediate temperature range. This chapter use theory and simulation to reproduce the fiber textures, and to identify the selection mechanisms that explain the origin of the actually observed patterns.

## 3.2 Introduction

Carbonaceous mesophase, such as coal tar and petroleum pitches are used in the industrial manufacturing of mesophase carbon fibers, using the melt spinning process [1]. The relatively newer carbon fiber manufacturing process results in fibers whose property profiles are competitive with those obtained from the conventional process based on acrylic precursors. The thermodynamic phase that describes carbonaceous mesophases is the

discotic nematic liquid crystal state. Liquid crystals are intermediate (i.e. mesophase) phases, typically found for anisotropic organic molecules, that exists between the higher temperature isotropic liquid state and the lower temperature crystalline state. (Detailed properties of nematic liquid crystals are provided in the classic textbooks on liquid crystal physics [2,3]). Carbonaceous mesophases are composed of disc-like molecules that align their unit-normals (i.e. vector perpendicular to the disc-like molecules) along a common direction, known as director **n**; see Figure 3-1. The name discotic distinguishes the molecular geometry and the name nematic identifies the type of liquid crystalline orientational order.

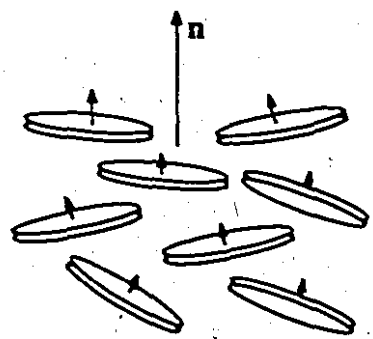


Figure 3-1: Orientational ordering in the uniaxial discotic nematic phase. The molecular normals of the randomly positioned disklike molecules partially orient along the director **n**.

The industrial fabrication of mesophase carbon fibers using the conventional melt spinning process [1] typically produces micrometer-sized cylindrical filaments whose cross-sectional area displays a variety of transverse textures, that is, different spatial arrangements of the average orientation **n** on the plane perpendicular to the fiber axis. The correlations between transverse textures and processing conditions, material properties, and geometry is a fundamental area of ongoing research in this field [4,5]. Among all the physical processing conditions, temperature is a fundamental factor that has been shown to have a significant effect on pattern selection [6]. Figure 3-2 shows a representative schematic of the orientation of fiber transverse textures adopted from [6], as well as some defining terminology to be discussed below. The left schematic shows that at

higher temperatures the fiber pattern adopts what is known as the onion texture, where the molecules are oriented in concentric circles. The right schematic shows that at lower temperatures the fiber pattern adopts what is known as the radial texture. In this texture the average molecular orientation follows radial trajectories. On the other hand, the middle schematic shows that at intermediate temperatures the pattern is isotropic and random.

The objective of this chapter is to use theory and simulation to reproduce and explain the sequence of temperature-driven fiber patterns transitions in melt-spun carbonaceous mesophases, as reported in [6], and shown in Fig. 3-2.

In order to specify the onion, radial and random patterns we next define some concepts and introduce the required terminology. In this chapter the mesophase carbon fiber is approximated by a monodisperse uniaxial discotic nematic liquid crystal [2], and the fiber spinning process is approximated by a steady, isothermal, incompressible, uniaxial extensional flow [7]. Using cylindrical coordinates $(r, \theta, z)$, the $z$ axis is along the fiber axis and the transverse plane is the $(r, \theta)$ plane. Here $0 < \theta < 2\pi$, and $r_i < r < r_o$, where $r_i$ is the radius of the inner core and $r_o$ is the radius of the fiber. The inner core radius $r_i$ represents the disclination line defect that runs along the fiber axis [3]. The triad $(\mathbf{e}_r, \mathbf{e}_\theta, \mathbf{e}_z)$ denotes the unit vectors in cylindrical coordinates, and the director field is: $\mathbf{n} = (n_r, n_\theta, n_z)$. Following previous study on similar pattern formation on discotic nematic liquid crystals [8], we assume that the director vector $\mathbf{n}$ has no $z$ component. That is, the director field $\mathbf{n}(r, \theta)$ is entirely confined within the $(\mathbf{e}_r, \mathbf{e}_\theta)$ plane, $\mathbf{n} = \mathbf{e}_r \cos(\phi) + \mathbf{e}_\theta \sin(\phi)$, here $\phi(r, \theta)$ is the director angle. Discotic nematics are elastic materials, where energy may be stored by orientation strains, this means that when $\nabla \mathbf{n} \neq 0$, elastic energy is stored. The two planar deformations for discotic nematics, identified as splay deformation and bend deformation, are characterized by two elastic constants $K_1$ and $K_3$, respectively. The radial texture of uniaxial discotic nematics, shown in Fig. 3-2, is defined by $n_\theta = 1(\phi = \frac{\pi}{2})$, and contains a pure bend mode. Similarly, the onion structure, shown in Fig. 3-2, is defined by $n_r = 1(\phi = 0)$, and contains a pure splay mode.

A fundamental feature of nematic elasticity is its anisotropy, which in this chapter

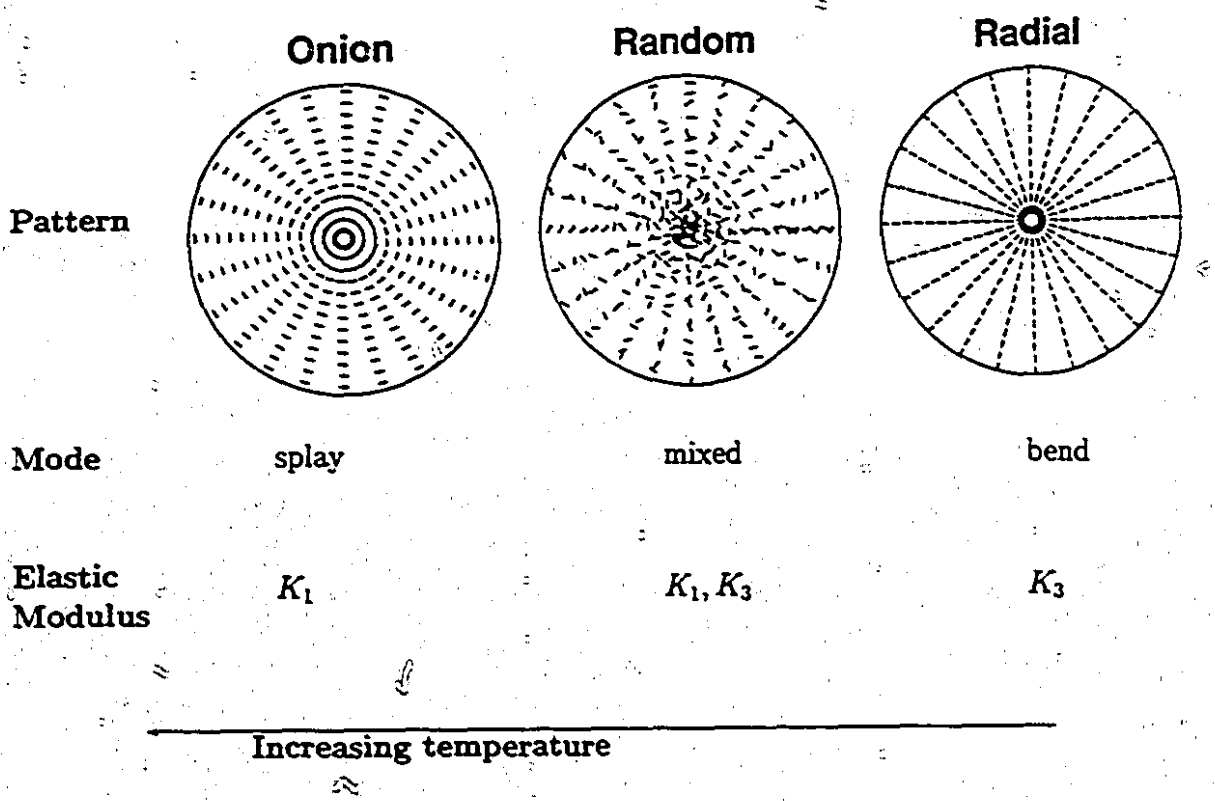


Figure 3-2: Schematics of the temperature dependence of transverse textures of actual mesophase carbon fibers, adopted from [6]. The radial pattern (left) is observed in fibers spun at lower temperatures, the onion pattern (right) at higher temperatures, and the random pattern (middle) in the intermediate temperature range. The elastic modulus and deformation mode are indicated below each pattern. The radial pattern consists of pure bend deformation ($K_3$), the onion pattern of pure splay ($K_1$), and the random pattern of a mixture of splay-bend deformation modes.

reduces to the statement $K_1 \neq K_3$. Since the elastic free energy is proportional to these moduli, and since these are temperature dependent, it is thus clear that temperature has a strong influence on the fiber pattern selection, if kinetic effects do not interfere with thermodynamics driving forces. The thermodynamics driving force in fiber texture selection is the minimization of the elastic free energy by avoidance of the high-modulus elastic mode. For example, if $K_1 > K_3$, elasticity selects the radial(bend) pattern over the onion(splay) pattern. Kinetic effects that may interfere with elasticity driven mechanisms are due to the viscous nature of liquid crystals, and hence with the required reorientation time $\tau_R$ as compared with the available process time $\tau_P$. If $\tau_P < \tau_R$ the initial texture may not reach the pattern selected by thermodynamics because there is simply not enough available time to achieve the required reorientation process.

As mentioned above the objective of this chapter is to reproduce and explain the origin of the pattern transitions shown in Fig. 3-2, as reported in [6]. The theory is based in the well-established classical equations of liquid crystal elasticity [3], known as Frank elasticity. This chapter is organized as follows. Section 2 presents the governing equations, discusses the temperature dependence of the parameters involved, and briefly describes the computational methods. Section 3 presents the numerical results and discussions. Finally, conclusions are presented.

## 3.3 Theory and formulation

In this section we present the basic equations that describe nematic liquid crystalline viscoelasticity, and follow the classical approach presented in [3]. The presentation is restricted to spatially homogeneous temperatures, incompressibility, and planar 2-D orientation (i.e. $\mathbf{n} = (n_r, n_\theta, 0)$). For planar orientation, the nematic free energy density is given by:

$$f = \frac{K_1}{2}(\nabla \cdot \mathbf{n})^2 + \frac{K_3}{2}(\mathbf{n} \times \nabla \times \mathbf{n})^2 \qquad (3.1)$$

where $K_1$ and $K_3$ are elastic constants defined above. In absence of external fields, the director field $\mathbf{n}$ is found by solving the torque balance equation [3]:

$$0 = \Gamma_i^{viscous} + \Gamma_i^{elastic}, (i = r, \theta, z) \tag{3.2}$$

where the viscous torque vector per unit volume $\Gamma^{viscous}$ and the elastic torque vector per unit volume $\Gamma^{elastic}$ are given by:

$$\Gamma^{viscous} = -\mathbf{n} \times (\gamma_1 \frac{d\mathbf{n}}{dt}), \; \Gamma^{elastic} = -\mathbf{n} \times \mathbf{h} \tag{3.3}$$

here $\mathbf{h}$ is the molecular field vector [3],

$$\begin{aligned} \mathbf{h} &= -\frac{\delta f}{\delta \mathbf{n}} \\ &= K_1 \bigtriangledown (\bigtriangledown \cdot \mathbf{n}) + K_3[\mathbf{B} \times \bigtriangledown \times \mathbf{n} + \bigtriangledown \times (\mathbf{n} \times \mathbf{B})] \end{aligned} \tag{3.4}$$

and $\mathbf{B} = \mathbf{n} \times \bigtriangledown \times \mathbf{n}$. Since $\mathbf{n} = (\cos\phi, \sin\phi, 0)$, the z-component of the viscous torque vector $\Gamma_z^{viscous}$ is given by:

$$\Gamma_z^{viscous} = -\gamma_1 \frac{d\phi}{dt} \tag{3.5}$$

For planar orientation the torques with respect to $\mathbf{e}_r$ and $\mathbf{e}_\theta$ play no role, and therefore the balance of elastic and viscousic torques leads to the single equation:

$$-\gamma_1 \frac{d\phi}{dt} + (\mathbf{n} \times \mathbf{h})_z = 0 \tag{3.6}$$

which is the governing equation in our study that describes the pattern selection process. Following Fig. 3-2, and without loss of generality we assume radial dependence, $\mathbf{n}(r,t) = (\cos\phi, \sin\phi, 0)$, with $\phi = \phi(r,t)$. In such case equation (3.6) becomes:

$$\gamma_1 \frac{d\phi}{dt} = (K_1 \sin^2\phi + K_3 \cos^2\phi)(\frac{\partial^2\phi}{\partial r^2} + \frac{1}{r}\frac{\partial\phi}{\partial r}) + (K_1 - K_3)\sin\phi\cos\phi(\frac{1}{r^2} + (\frac{\partial\phi}{\partial r})^2) \tag{3.7}$$

As Fig. 3-2 shows, the actual pattern selection is driven by temperature effects on material parameters. Hence to eliminate boundary constraints as sources of texture transitions,

we use the following Neumann type of boundary conditions: $\frac{\partial\phi}{\partial r}|_{r=r_i} = \frac{\partial\phi}{\partial r}|_{r=r_o} = 0$. In all computations an initial random orientation is adopted. To generate the random orientation, we use a in-built random number generator to produce the director angle $\phi$. Although the actual director orientation at the beginning of the spinnline is not known, the random state adopted here eliminates any bias or preference of one texture over another, thus helping to elucidate the operating driving force for pattern formation in the spinnline.

The essential hypothesis of this chapter that is sufficient and necessary to explain the pattern transition shown in Fig. 3-2 is that the elastic constants exhibit a cross-over at an intermediate temperature $T_c$ at which the material is elastically isotropic. Thus we assume that:

$$T < T_c \quad , \quad K_1 > K_3 \tag{3.8}$$

$$T = T_c \quad , \quad K_1 = K_3 = K \tag{3.9}$$

$$T > T_c \quad , \quad K_1 < K_3 \tag{3.10}$$

Such temperature driven cross-over of Frank elastic constants has been measured for rod-like nematic liquid crystals [10]. The situation for disc-like nematics (carbonaceous mesophases) is identical with that of rods if we reverse the meaning of $K_1$ and $K_3$, since bending (splaying) discs correspond to splaying (bending) rods. Thus the temperature dependence and cross-over adopted in this chapter is perfectly consistent with actual measurements.

The dimensionless form of equation (3.7) is obtained by dividing both sides with $(\frac{K}{r_o^2})$. Equation (3.7) then becomes:

$$\frac{d\phi}{d\tilde{t}} = (\alpha \sin^2\phi + \beta)(\frac{\partial^2\phi}{\partial\tilde{r}^2} + \frac{1}{\tilde{r}}\frac{\partial\phi}{\partial\tilde{r}}) + \alpha \sin\phi\cos\phi(\frac{1}{\tilde{r}^2} + (\frac{\partial\phi}{\partial\tilde{r}})^2) \tag{3.11}$$

where $\tilde{r}$ is the dimensionless radius ($\tilde{r} = \frac{r}{r_o}$), and $\tilde{t}$ is the dimensionless time ($\tilde{t} = \frac{t}{\zeta}$), $\zeta$ is the reorientation time constant given by $\zeta = \frac{\gamma_1 r_o^2}{K}$, $\alpha = \frac{K_1 - K_3}{K}$, and $\beta = \frac{K_3}{K}$. For simplicity, in what follows we drop the tildes and use $r$ to represent $\tilde{r}$, and $t$ to represent

$\tilde{t}$.

In the equation (3.11), we separate the linear terms from the nonlinear terms and rewrite equation (3.11) as:

$$\frac{d\phi}{dt} = \beta(\frac{\partial^2\phi}{\partial r^2} + \frac{1}{r}\frac{\partial\phi}{\partial r}) + \alpha[\sin^2\phi(\frac{\partial^2\phi}{\partial r^2} + \frac{1}{r}\frac{\partial\phi}{\partial r}) + \sin\phi\cos\phi(\frac{1}{r^2} + (\frac{\partial\phi}{\partial r})^2)] \tag{3.12}$$

The dimensionless equation (3.12) is a nonlinear parabolic partial differential equation that gives the director orientation as a function of position and time, for a given set of parameters: $\phi = \phi(r, t, \alpha, \beta)$, where $-\infty < \alpha < \infty$ and $\beta > 0$. We can now restrict equation (3.12) to the three representative cases shown in Fig. 3-2:

(i) Radial pattern: $K_1 > K_3$, $\alpha > 0$;

(ii) Random pattern: $K_1 = K_3$, $\alpha = 0$;

(iii) Onion pattern: $K_1 < K_3$, $\alpha < 0$.

In the case of elastic isotropy $\alpha = 0$, equation (3.12) becomes linear. The right hand side of this equation ($\beta\frac{1}{r}\frac{\partial}{\partial r}(r\frac{\partial\phi}{\partial r})$) represents the driving force that at steady state leads to minimization of the free energy for $K_1 = K_3$:

$$F = \frac{K}{2}[(\nabla\cdot\mathbf{n})^2 + (\nabla\times\mathbf{n})^2] \tag{3.13}$$

Thus when the material is elastically isotropic ($K_1 = K_3$) the pattern will evolve to minimize the divergence and the curl of $\mathbf{n}$, and elasticity, in the absence of boundary constraints, will select the onion pattern or the radial pattern with equal probability since in both cases the total free energy are the same, and it is given by:

$$T = T_c, \quad F = K\pi\ln(\frac{r_o}{r_i}) \tag{3.14}$$

On the other hand, the actual case is that of elastic anisotropy $\alpha \neq 0$. Now the elastic anisotropy introduces nonlinear terms (the second part of the right hand side in equation (3.12)) that leads, as shown below, to a distinction between the energetic contexts of the onion and radial patterns, and thus provides a driving force for pattern selection.

We have numerically integrated equation (3.12) using the Galerkin Finite Element

method [9], with a corrector-predictor adaptive time integration step. The spatial discretization uses 100 quadratic elements. The discretized equation were solved using Newton-Raphson iterations. To estimate the time required to reach steady state we proceed as follows. The time steps are determined according to the change of director field, measured by the norm of the difference of the director field vector at consecutive time steps $\Delta\phi = |\|\phi^{n+1}\| - \|\phi^n\||$. When the norm is sufficiently small (here the threshold is given by $\Delta\phi < 10^{-6}$), we consider that the system has reached the steady state, and thus calculate the estimated time in which the director field changes from a random initial state to the final steady state. We denote this time by $\tau_\alpha$, where the subscript $\alpha$ indicates that $\tau_\alpha$ is a function of the parameter $\alpha$; $\tau_0$ corresponds to $\alpha = 0$, that is when $T = T_c$ (see equation (9)).

## 3.4 Results and discussions

This section presents the solutions to equation (3.12), and discusses them in reference to Fig. 3-2. The results are naturally presented in three categories for three representative temperature ranges, taking into account the elastic constant inequalities shown in equations (3.8-3.10). The computed numerical results of the director orientation angle $\phi(r,t)$ profiles are converted into scientific visualizations, shown as thin line segments (as in Fig. 3-2). Each segment represents at the given $(r,t)$ the average disc orientation. Without loss of generality we assume a linear dependence of the elastic constants on temperature. The cross over of the two dimensionless elastic constants $(\frac{K_1}{K}, \frac{K_3}{K})$ as a function of dimensionless temperature $\frac{T}{T_c}$ is shown in Fig. 3-3. The thermal sensitivity of the elastic anisotropy shown in Fig. 3-3 contains the necessary and sufficient features identified in equations (3.8-3.10).

(i) **Radial pattern**

The radial pattern consists of pure bend deformation ($\phi = \frac{\pi}{2}, n_0 = 1$). This pattern is selected when $K_1 > K_3$, $\alpha > 0$. This is clear when comparing the total free energy of

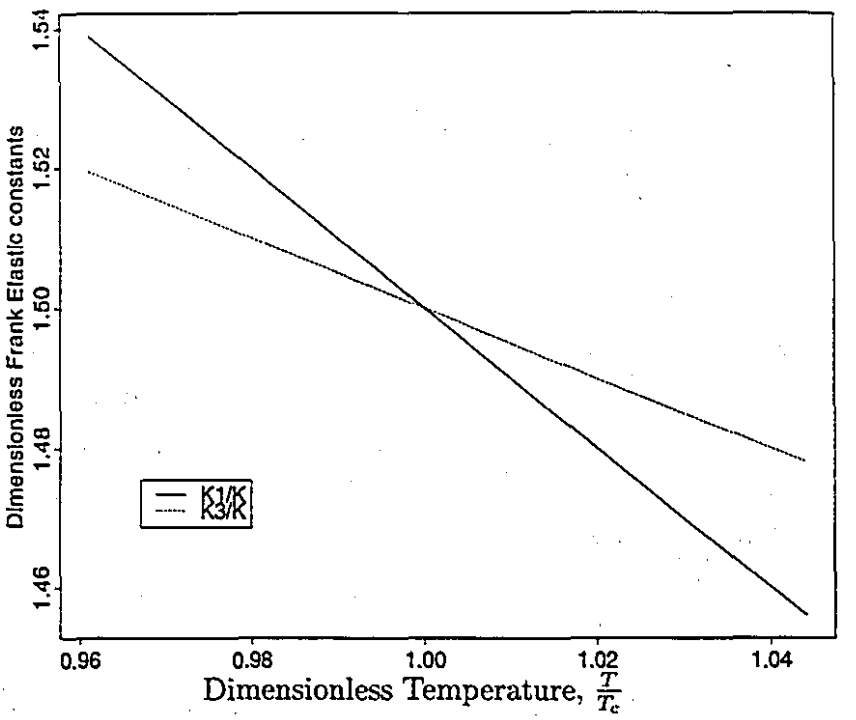


Figure 3-3: A simplified linear representation of the scaled elastic constants $(\frac{K_1}{K}, \frac{K_3}{K})$ cross-over as a function of dimensionless temperature $\frac{T}{T_c}$. The constants $K_1$ and $K_3$ are scaled with $K$, which is the cross point of $K_1$ and $K_3$. The temperature is scaled by the transitional temperature $T_c$ at which $K_1 = K_3$. Such temperature dependence has been found in rod-like nematic liquid crystals [10].

the onion $F^o$ and radial $F^r$ patterns:

$$F^o = K_1 \pi \ln(\frac{r_o}{r_i}) \tag{3.15}$$

$$F^r = K_3 \pi \ln(\frac{r_o}{r_i}) \tag{3.16}$$

Thus it is clear that when $K_1 > K_3$, $F^r < F^o$ and the radial pattern is energetically favorable. Figure 3-4 shows a computed visualization of one fourth of the fiber cross-section texture for an initially random orientation (left schematic) and at steady state (right schematic), for $\alpha = 0.1$ and $\beta = 1$. The figure clearly shows the selection the radial pattern from an initially random state when $K_1 > K_3$.

(ii) **Onion pattern**

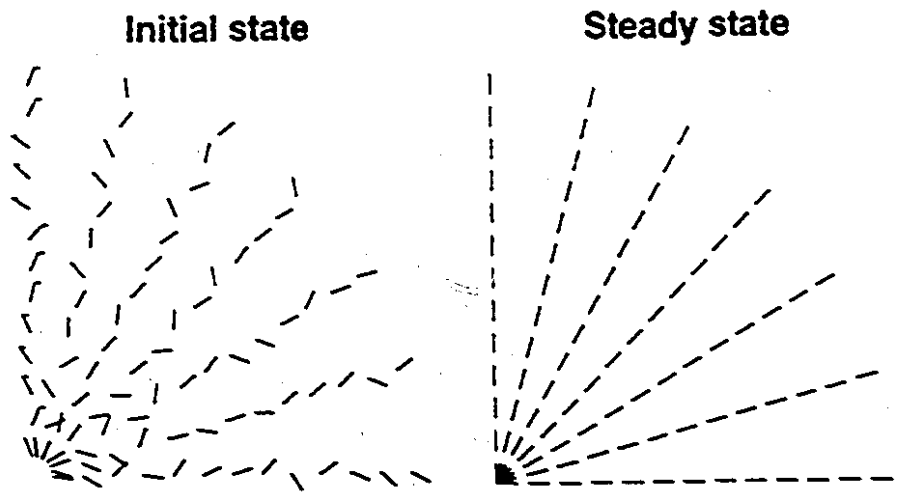


Figure 3-4: Computed scientific visualization of the cross-section fiber texture, for $\alpha = 0.1, \beta = 1$. When $K_1 > K_3$, the most favorable elastic deformation is bend, the system will evolve to radial (pure bend) pattern at equilibrium.

The onion pattern consists of a pure splay deformation ($\phi = 0, n_r = 1$) and is naturally selected for an initially random state whenever $K_1 < K_3$ ($\alpha < 0$). For the assumed temperature dependence given in equations (3.8-3.10), this occurs at relatively higher temperatures. Figure 3-5 shows a visualization of one fourth of the fiber cross-section texture for $\alpha = -0.1$ and $\beta = 1$. The figure shows that the steady state solution to equation (3.12) for $K_1 < K_3$ is the onion pattern.

(iii) **Random pattern**

As $\alpha$ approaches zero from either below or above, the numerical solutions remain either pure splay or pure bend, according to the different values of $\alpha$, but the convergence rate slows down drastically as $\alpha \to 0$. Nevertheless, as long as $K_1$ and $K_3$ remain different from each other, the steady state solution always reflects the lowest free energy mode in accordance with the elastic anisotropic condition. From the numerical solutions of equation (3.12) presented above, we may conclude that due to the elastic anisotropy, the free energy minimization will rearrange the director orientation such that the director field at equilibrium will have the lowest free energy. In general, the results are in agreement with the experimental observation shown in Fig. 3-2. However, the origin of the random pattern observed in the transitional temperature range remains unclear. To explain the

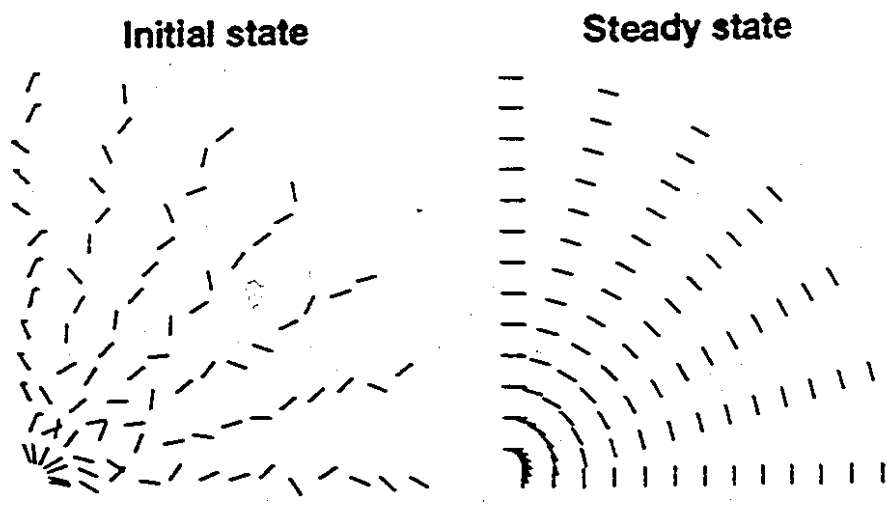


Figure 3-5: Computed scientific visualization of the cross-section fiber texture, for $\alpha = -0.1, \beta = 1$. When $K_1 < K_3$, the most favorable elastic deformation is splay, therefore the system will evolve to the onion (pure splay) pattern at equilibrium.

origin of the random pattern, we take in account the kinetics of the system characterized by $\tau_\alpha$ (defined in the previous section).

Figure 3-6 shows the computed dimensionless director reorientation time $\frac{\tau_\alpha}{\tau_0}$ as a function of dimensionless temperature $\frac{T}{T_c}$. As $\alpha \to 0$ $(T \to T_c)$, the simulations show that the time needed for the director field to reach the equilibrium increases significantly. Figure 3-7 shows the one dimensional visualization of the change of director orientation in the radial direction as a function of dimensionless time $t$, for $\alpha = -0.1$. At $t = 11.58$ the system undergoes very little change from the previous time step and therefore we conclude that the system has reached equilibrium. Figure 3-8 shows the one dimensional visualization of the director orientation for $\alpha = -0.01$. By comparing Fig. 3-7 with Fig. 3-8, we can see the director reorientation slows down by a factor of 10. At $\alpha = 0$, equation (3.12) becomes:

$$\frac{d\phi}{dt} = \frac{\partial^2 \phi}{\partial r^2} + \frac{1}{r}\frac{\partial \phi}{\partial r} \tag{3.17}$$

Solving the above equation, we obtain the director field $\phi$ as a function of $t$ and $r$:

$$\phi = \sum_{n=1}^{\infty} A_n J_0(\lambda_n r) e^{-\lambda_n t} \tag{3.18}$$

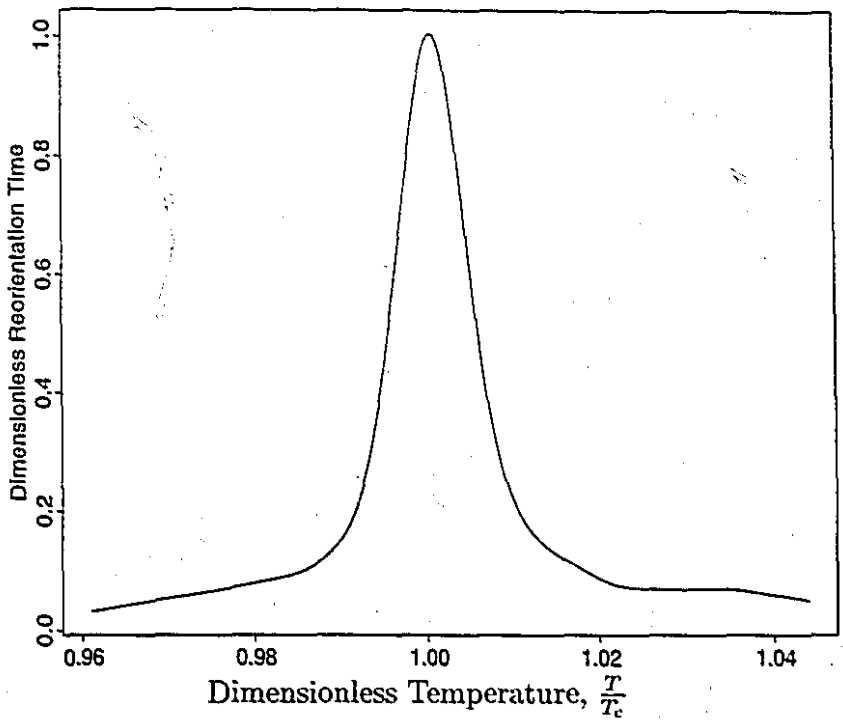


Figure 3-6: Dimensionless reorientation time $\frac{\tau_\alpha}{\tau_0}$ as a function of dimensionless temperature $\frac{T}{T_c}$, corresponding to the temperature dependence shown in Fig. 3-3. The dimensionless reorientation time $\tau_\alpha$ is scaled by the reorientation time at the transtional temperature $T_c$. The reorientation time sharply increases as the temperature difference $|T - T_c|$ decreases. At $T = T_c$ the reorientation is the slowest.

here $A_n$ is the coefficients, $J_0$ is zeroth order Bessel function. The eigenvalues $\lambda_n$ are determined by the boundary condition at $r = 1$, and are the zero points of the first order Bessel function $J_1(\lambda_n) = 0$. The linear terms in the above equation represents the minimizing of divergence $(\nabla \cdot \mathbf{n})$ and curl $(\nabla \times \mathbf{n})$ terms of the free energy at $K_1 = K_3$. This minimizing process is independent of the elastic anisotropy and exists in all cases. Together with the elastic anisotropy, represented by the nonlinear terms in equation (3.12), they consist of the driving force behind the pattern selection mechanism in fiber spinning process. If we consider the the state of liquid crystal material to be random, under the influence of the driving force described above, the fiber will rearrange its director field to reduce the free energy while at the same time being cooled down. Such microscopic process is normally sufficiently fast in the process time scale. However, as $\alpha \to 0$, the

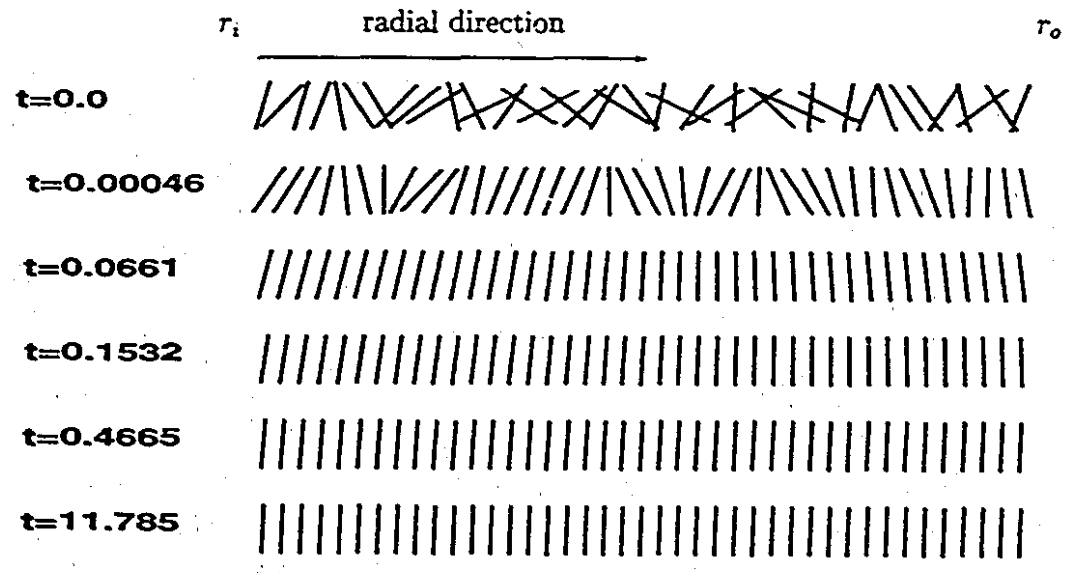


Figure 3-7: One dimensional scientific visualization of the director field in the radial direction for $\alpha = 0.1$. The initial state is given by a random director angle. Director fields are shown for several increasing times. For $\alpha = 0.1$, the final equilibrium is the onion pattern, which agrees with the result from steady state solutions.

kinetics of the system undergoes a significant slowing down , that is, the time needed to rearrange the director field to reach the equilibrium state becomes much longer as the system approaches the transitional temperature $T_c$. The reason for such slowing down is that because at the transitional temperature $T_c$ the elastic anisotropic is very weak ($\alpha \approx 0$), the energetic superiority of one deformation mode over the other becomes very small, which greatly weakens the driving force effect of elastic anisotropy on the pattern selection. Because of the slowing down, the effect of minimizing the divergence and curl of the director orientation field becomes the major contributor to the pattern selection. The effect of such minimization is of small magnitude when compared with the effect of

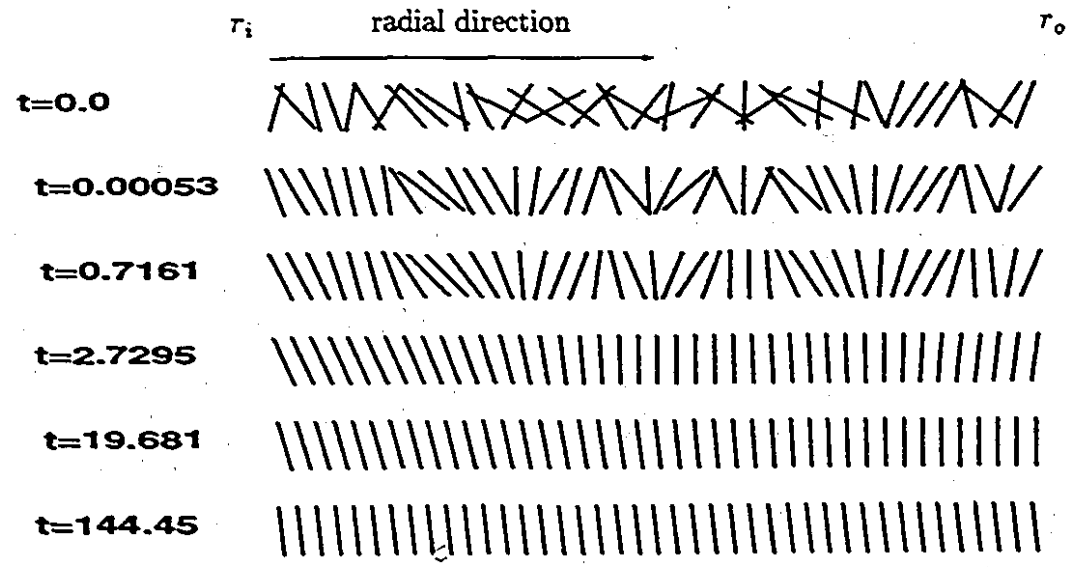


Figure 3-8: One dimensional scientific visualization of the director field in the radial direction for $\alpha = 0.01$. The initial state is given by a random director angle. Director fields are shown for several increasing times. Comparing to the director reorientation process shown in Fig. 3-7, the reorientation time has increased by a factor of ten as $\alpha$ decreases from 0.1 to 0.01. The final equilibrium is the onion pattern, which agrees with the result from steady state solutions.

the elastic anisotropy that exists when the temperature $T$ is sufficietly different from $T_c$. As a result, driven mostly by this minimization force, the director reorientation process becomes much slower. Since the fiber spinning process time is fixed for all temperatures, the director reorientation time at the transitional temperature would become much longer than the fiber spinning process time. Sufficiently close to the transition temperature the fiber is solidified before it can reach an orderly pattern, and the random pattern is then observed.

## 3.5 Conclusion

In summary, we have presented a simple analysis to a complex process that is able to explain, using well known theory of liquid crystal materials, the formation of transverse textures observed at different temperatures in the experimental fiber spinning process of cabonaceous mesophases. The numerical results presented above show that the pattern formation in the fiber spinning process is explained by the minimization of elastic free energy. The cross-over of the elastic constants changes the most favorable free energy mode from bend at lower temperatures to splay at higher temperatures, and causes the switch from the radial pattern to the onion pattern. However, as the temperature approaches the transitional temperature at which the material is elastically isotropic, the director reorientation time increases sharply and exceeds the fiber spinning process time, and thus structuring does not occur, and hence no distinctive pattern arises. The random pattern is the result of such slowing down in the director reorientation.

# Bibliography


[1] Peebles L.H.Jr., *Carbon Fibers-Formation, Structure, And Properties* (CRC Press, Boca Raton, 1995).

[2] Chandrasekhar S., *Liquid Crystals*, 2nd ed. (Cambridge University Press, Cambridge, 1992).

[3] de Gennes P.G. and Prost J., *The Physics of Liquid Crystals*, 2nd ed. (Clarendo, Oxford, 1993).

[4] Fatholahi B. and White J.L., J.Rheol. **38**, 1951(1994).

[5] McHugh J.J. and Edie D.D., Liquid Crystals **18**, 327(1995).

[6] Otani S. and Oya A., Progress of pitched-based carbon fiber in Japan, *Petroleum Derived Carbons*, Bacha J D, Newman J W and White J L, Eds., ACS Symp. Ser. No. 303, American Chemical Society, Washington, D.C., 322, 1986.

[7] Bird R.B., Curtiss C.F., Armstrong R.G. and Hasager O., *Dynamics of Polymeric Liquids* (Wiley, New York, 1987), Vol 1.

[8] Rey A.D., Phys. Rev. E, **51**, 6278(1995).

[9] Carey G. and Oden J.T., *Finite Elements* (Prentice-Hall, Englewood Cliffs, NJ, 1983).

[10] Karat P.P. and Madhusudana N.V., Mol. Cryst. Liq. Cryst. **40**, 239(1977).

# Chapter 4

# Conclusion

This thesis presents a comprehensive characterization of orientation development in the cross-section of discotic nematic liquid crystalline fibers subjected to isothermal, incompressible, uniaxial extensional (spinning) flow, using theory and simulation. The thesis shows that the main structuring effect arising from the extensional flow is to produce a degenerate planar orientation. The degenerate flow-induced planar orientation pattern is resolved by mechanisms arising from the elastic nature of the simulated discotic nematic liquid crystalline material. All numerical and analytical results presented in this thesis show that the factor governing the selection of distinct fiber structures in extensional flows is induced by the minimization of the elastic free energy. All the results presented in this thesis were validated using extensively available experimental data, representative of actual fibers produced during the industrial spinning of carbonaceous mesophases. The validation process is based on a comparison of the scientific visualization of the model output variables with micrographs of fiber cross-sectional textures. The results of the validation process indicated that the simulations are able to capture and explain the origin of the most common fiber textures observed in the industrial spinning of carbonaceous mesophases. Below we summarize details of the findings for the specific patterns that were successfully reproduced in this study.

The oscillatory zig-zag fiber texture has been found to emerge as a preferred pattern whenever the elastic anisotropy favors splay deformations while the boundary orientation favors bend deformations. Under such conditions bend deformations are avoided by the

appearance of orientation oscillations, which successfully replace bend by splay. Using computational bifurcation methods as well as functional analysis techniques we identified the spatially oscillatory solutions as solution branches arising from unstable spatially homogeneous solutions. The multi-branching sequence at the multiple-eigenvalues of the bifurcation equation was captured using both analysis and numerical simulation. Bifurcation, amplitude, and stability diagrams provide the correlations between process conditions, material properties, and selected fiber texture. The second major contribution of this thesis is the elucidation of the mechanisms that control the temperature-driven fiber texture transitions involving the radial, onion, and random patterns. The present work has shown that for materials that exhibit a cross-over in the splay and bend elastic constants as a function of temperature will exhibit the texture transitions indicated above. Far away from the transition point minimization of the elastic free energy is an efficient driving force that gives rise to the selection of onion pattern at higher temperatures and radial pattern at lower temperatures. In addition, it is shown that sufficiently close to the temperature at which the material becomes elastically isotropic, the kinetics of the pattern selection process slows down significantly. The lack of available time for a definite pattern structure to emerge, thus results in a random pattern. The thermodynamic and kinetic mechanisms thus explain the origin of the patterns and the transition of textures, observed during the industrial spinning of carbonaceous mesophases.

# Appendix A

The objective of this appendix is to present the mathematical analysis that correlates the eigenvalue problem (2.22) with the bifurcations of equation (2.9). First we introduce the required nonlinear functional analysis concepts. A nonlinear mapping $\mathbf{G}$ from a Banach space $\mathbf{H}$ to $\mathbf{K}$ is said to be *Fréchet* differentiable at a point $v$ provided there is a bounded linear operator $\mathbf{A}$ from $\mathbf{H}$ to $\mathbf{K}$ such that the quantity $R(v;h) = \mathbf{G}(v+h) - \mathbf{G}(v) - \mathbf{A}h$ is $o(h)$ as $h \to 0$; that is

$$\lim_{\|h\| \to 0} \frac{\| R(v;h) \|}{\| h \|} = 0. \tag{A.1}$$

We denote the Fréchet derivative of $\mathbf{G}$ at $v$ by $\mathbf{G}'(v)$ or by $\mathbf{G}_v$; when it exists it may be found by the usual formula of

$$\mathbf{G}'(v)h = \lim_{t \to 0} \frac{\mathbf{G}(v+th) - \mathbf{G}(v)}{t} = \frac{d}{dt}\mathbf{G}(v+th) \mid_{t=0} . \tag{A.2}$$

For a nonlinear equation

$$\mathbf{G}(\phi, \mu) = 0 \tag{A.3}$$

where $\mathbf{G}$ is a differentiable mapping between two Banach spaces $\mathbf{H}$ and $\mathbf{K}$, that is, $\mathbf{G} : \mathbf{H} \times \Lambda \to \mathbf{K}$, where $\Lambda$ is a finite dimensional parameter space. Suppose the operator $\mathbf{G}$ has an equilibrium solution of $(\phi_0, \mu_c)$ at which

$$\mathbf{G}(\phi_0, \mu_c) = 0 \tag{A.4}$$

Whether the solution $(\phi_0, \mu_c)$ is a bifurcation point is given by the following *Implicit Function Theorem* [21].

**Implicit Function Theorem 1** *With the definition of the Banach space* $\mathbf{H}$, $\mathbf{K}$ *and the operator* $\mathbf{G}$ *given above we assume that* $\mathbf{G}$ *is Fréchet differentiable. The Fréchet derivative of* $\mathbf{G}$ *at* $(\phi_0, \mu_c)$, *designated by* $\mathbf{G}_\phi(\phi_0, \mu_c)$ *is a linear mapping* $\mathbf{G}_\phi : \mathbf{H} \to \mathbf{K}$. *If* $\mathbf{G}_\phi(\phi_0, \mu_c)$ *possesses a bounded inverse, then locally for* $|\mu - \mu_c|$ *sufficient small, there exists a differentiable mapping* $\phi(\mu)$ *from* $\Lambda$ *to* $\mathbf{H}$, *with* $(\phi(\mu), \mu) \subset \mathbf{H} \times \Lambda$, *such that* $\mathbf{G}(\phi(\mu), \mu) = 0$. *Furthermore, in a sufficient small neighborhood of* $(\phi_0, \mu_c)$, $(\phi(\mu), \mu)$ *is the only solution to* $\mathbf{G} = 0$.

From the Implicit Function Theorem, it follows that if $\mathbf{G}$ vanishes at $(\phi_0, \mu_c)$ and $\mathbf{G}_\phi$ is invertible there, then there is a locally smooth curve $\phi(\mu)$ through $(\phi_0, \mu_c)$, and this curve of $\phi(\mu)$ is the unique solution of $\mathbf{G}$ at this point. Therefore a bifurcation can only occur, if the linear mapping of $\mathbf{G}_\phi$, evaluated at $(\phi_0, \mu_c)$, is singular and hence for a linear mapping $\mathbf{A} := \mathbf{G}_\phi(\phi_0, \mu_c) : \mathbf{H} \to \mathbf{K}$ there is no inverse. If the above condition is met, one can conclude that the solution $(\phi_0, \mu_c)$ is a bifurcation point. We rewrite the equation (2.9) as

$$G(\phi, \mu) = \phi'' - \frac{(-\mu + 1)\sin\phi\cos\phi(1 + \phi'^2)}{\mu\sin^2\phi + \cos^2\phi} = 0 \tag{A.5}$$

with the boundary conditions:

$$\phi(0) = \phi(u_o) = \frac{\pi}{2}. \tag{A.6}$$

Introducing the linear transformation $\phi = \frac{\pi}{2} + \delta$, we have

$$G(\delta, \mu) = \delta'' + \frac{(-\mu + 1)\sin\delta\cos\delta(1 + \delta'^2)}{\mu\cos^2\delta + \sin^2\delta} = 0 \tag{A.7}$$

with homogeneous boundary conditions

$$\delta(0) = \delta(u_o) = 0. \tag{A.8}$$

The above equation has a trivial solution of $\delta_0 = 0$, for all values of $\mu$. To examine the stability of the trivial solution $\delta_0$, we shall find values of $\mu$, for which the linear mapping $A = G(\delta_0, \mu)$ does not have an inverse. Hence we must look for the nontrivial solution

of the corresponding eigenvalue problem. The linear operator is obtained by taking the Fréchet derivative of (A.7)

$$A\delta = G_\delta(\delta_0, \mu)\delta = \delta'' - \frac{2(1+\delta_0'^2)(1-2\mu+\mu^2-\cos(2\delta_0)+\mu^2\cos(2\delta_0))}{(1+\mu-\cos(2\delta_0)+\mu\cos(2\delta_0))^2}\delta. \qquad (A.9)$$

Inserting the trivial solution $\delta_0 = 0$ into this equation, we obtain the linear eigenvalue problem

$$G_\delta(0,\mu)\delta = \delta'' + (\frac{1}{\mu} - 1)\delta = 0 \qquad (A.10)$$

with the boundary conditions $\delta(0) = \delta(u_o) = 0$. The general solution of the eigenvalue problem is given by:

$$\delta(u) = B\cos(\sqrt{\frac{1}{\mu} - 1}u) + D\sin(\sqrt{\frac{1}{\mu} - 1}u) \qquad (A.11)$$

The boundary condition $\delta(0) = 0$ implies that $B = 0$, so $\delta(u_o) = 0$ gives the eigenvalue $\mu$:

$$\frac{1}{\mu} - 1 = (\frac{n\pi}{\Delta u})^2 \qquad (A.12)$$

which gives

$$\mu_{c,n} = \frac{1}{1+(\frac{n\pi}{\Delta u})^2}, (n = 1, 2, \ldots) \qquad (A.13)$$

and the corresponding eigenfunctions are

$$\delta_n = D_n \sin(\frac{n\pi}{\Delta u}u), (n = 1, 2, \ldots). \qquad (A.14)$$

Here $D_n$ are arbitrary constants which can not be determined from the conditions given above. Now we consider equation (2.22)

$$\frac{K_1 - K_3}{2}\delta - \frac{K_1}{2}\delta'' = \lambda\delta \qquad (A.15)$$

which when dividing by $K_1$ gives:

$$\delta'' + \{\frac{2\lambda}{K_1} - (1 - \frac{1}{\mu})\}\delta = 0 \qquad (A.16)$$

Since we are looking for $\lambda > 0$, the critical values of $\mu_c$ are to be found by setting $\lambda = 0$. Then the above equation becomes identical to equation (A.10). So we proved that equation (2.22) is the Fréchet derivative of equation (2.9) after the linear transformation (2.18). Following the Implicit Function Theorem and the discussion, we can now conclude that the branch of the trivial solution ($\delta = 0$, or $\phi = \frac{\pi}{2}$) has multiple bifurcations at the eigenvalues shown above. At the eigenvalues, the linear mapping of $G_\delta$ in (A.10) becomes singular and doesn't have an inverse. It follows that the nonlinear operator of $G$ will have nontrivial solutions in the neighborhood of $\mu_{c,n}$. At the bifurcation points $\mu_{c,n}$, the nontrivial solution to the linear mapping of $G_\delta$ are the eigenfunctions (A.14) then we have

$$\phi_n = \delta_n + \frac{\pi}{2} = D_n \sin(\frac{n\pi}{\Delta u}u) + \frac{\pi}{2}, (n = 1, 2, \ldots). \tag{A.17}$$

For $n = 1$, $\Delta u = 1$ and $\mu_{c,1} = 0.092$, we have the nontrivial solution of

$$\phi_1 = D_n \sin(\pi u) + \frac{\pi}{2}, \tag{A.18}$$

which has half wave length and matches the numerical solution found at $\mu_{c,1}$. Continuing this process for larger $n$, we find that each eigenfunction matches the numerical solution at that point of $\mu_{c,n}$. Using the Ljapunov-Schmidt method [21], we can decompose $\delta$ in the form:

$$\delta = \delta_c + \delta_s \tag{A.19}$$

where

$$\delta_c = q \sin(\frac{n\pi}{\Delta u}u) \tag{A.20}$$

and

$$\delta_s = h(q, u) \tag{A.21}$$

In (A.20), $q$ is the amplitude of the oscillatory solution. And $h = O(q^2)$ [21].

Linearizing equation (A.7) and projecting it onto the eigenfunctions, we find:

$$\int_0^{u_o} [\delta'' + \lambda(\delta + \delta\delta'^2)] \sin(\frac{n\pi}{\Delta u}u) du = 0 \tag{A.22}$$

Here $\lambda = (\frac{1}{\mu} - 1)$. Substituting (A.19) into the above integral, we find:

$$\int_0^{u_o} [q(-\frac{n^2\pi^2}{(\Delta u)^2} + \lambda)\sin(\frac{n\pi}{\Delta u}u) + h'' + \lambda h$$
$$+\lambda(q^3\frac{n^2\pi^2}{(\Delta u)^2}\sin(\frac{n\pi}{\Delta u}u)\cos^2(\frac{n\pi}{\Delta u}u)) + o(q^3)]\sin(\frac{n\pi}{\Delta u}u)du = 0 \qquad (A.23)$$

If we substitute $\lambda = \lambda_n$, the linear terms in $q$ in (A.23) vanish. Furthermore, since $h$ is orthogonal to the eigenfunctions, we have:

$$\int_0^{u_o} (h'' + \lambda h)\sin(\frac{n\pi}{\Delta u}u)du = 0 \qquad (A.24)$$

Therefore, after neglecting higher order terms, the integral (A.23) becomes:

$$\int_0^{u_o} [q(-\frac{n^2\pi^2}{(\Delta u)^2} + \lambda)\sin(\frac{n\pi}{\Delta u}u)$$
$$+\lambda(q^3\frac{n^2\pi^2}{(\Delta u)^2}\sin(\frac{n\pi}{\Delta u}u)\cos^2(\frac{n\pi}{\Delta u}u))]\sin(\frac{n\pi}{\Delta u}u)du = 0 \qquad (A.25)$$

After integrating, we have:

$$\frac{q(\lambda - \lambda_n)}{2} - \frac{\lambda}{\lambda_n}\frac{q^3}{4} = 0 \qquad (A.26)$$

Therefore in a small neighborhood of $\lambda_n$ ($\lambda \approx \lambda_n$), the solution amplitude $q$ and $\lambda$ have the following relationship:

$$q = \sqrt{2(\lambda - \lambda_n)}, (n = 1, 2, \ldots) \qquad (A.27)$$

Since $\lambda = (\frac{1}{\mu} - 1)$, we find that sufficiently close to the bifurcation point, the amplitude $q$ and the elastic anisotropy $\mu$ are related by:

$$q = \sqrt{2\frac{\mu_{c,n} - \mu}{\mu\mu_{c,n}}}, (n = 1, 2, \ldots) \qquad (A.28)$$

Equation (A.28) predicts that close to a bifurcation of order $n$, the amplitude of the $n$th mode grows at a faster(slower) rate for larger(smaller) $n$. This is in agreement with the numerical results shown in Fig.8; by comparing curve A ($n = 1$) with curve C ($n = 3$)

we see that the amplitude grows faster in the latter case.

In summary, the contents of this appendix shows the mathematical analysis that explains the multiple bifurcations at eigenvalues. By applying the Ljapunov-Schmidt method [21], we also derive the relationship between the solution amplitude and the elastic anisotropy.